

Scattering approach to diffusion quantifies axonal damage in brain injury

Ali Abdollahzadeh,^{1,2,*} Ricardo Coronado-Leija,¹ Hong-Hsi Lee,³

Alejandra Sierra,² Els Fieremans,¹ and Dmitry S. Novikov¹

¹Center for Biomedical Imaging, Department of Radiology,
New York University School of Medicine, New York, NY, USA

²A.I. Virtanen Institute for Molecular Sciences, University of Eastern Finland, Kuopio, Finland

³Athinoula A. Martinos Center for Biomedical Imaging, Department of Radiology,
Massachusetts General Hospital, Harvard Medical School, Boston, MA, USA

Early diagnosis and noninvasive monitoring of neurological disorders require sensitivity to elusive cellular-level alterations that occur much earlier than volumetric changes observable with the millimeter-resolution of medical imaging modalities. Morphological changes in axons, such as axonal varicosities or beadings, are observed in neurological disorders, as well as in development and aging. Here, we reveal the sensitivity of time-dependent diffusion MRI (dMRI) to axonal morphology at the micrometer scale. Scattering theory uncovers the two parameters that determine the diffusive dynamics of water in axons: the average reciprocal cross-section and the variance of long-range cross-sectional fluctuations. This theoretical development allowed us to predict dMRI metrics sensitive to axonal alterations across tens of thousands of axons in seconds rather than months of simulations in a rat model of traumatic brain injury. Our approach bridges the gap between micrometers and millimeters in resolution, offering quantitative, objective biomarkers applicable to a broad spectrum of neurological disorders.

Neurological disorders are a global public health burden, with their prevalence expected to rise as the population ages [1]. A ubiquitous signature of a wide range of these pathologies is the change in axon morphology at the micrometer scale. Such changes are extensively documented in Alzheimer's [2, 3], Parkinson's [4, 5], and Huntington's [6, 7] diseases, multiple sclerosis [8–10], stroke [11–13], and traumatic brain injury (TBI) [14–16]; they are also implicated in development [17, 18] and aging [19, 20]. In particular, within neurodegenerative disorders [2–7], abnormalities in the axon morphology involve disruptions in axonal transport [21–24] and the aberrant accumulation of cellular cargo [23, 24] comprising mitochondria, synaptic vesicles, or membrane proteins and enzymes [22]. This buildup forms a transport jam, often presenting itself in terms of axonal varicosities or beadings [2, 5, 21, 25], contributing to abnormal morphological changes along axons — a unifying microstructural disease hallmark, notwithstanding the wide heterogeneity of clinical symptoms.

Detecting and quantifying the key micrometer-scale changes [3, 25–29] that precede macroscopic atrophy or edema, are unmet clinical needs and technological challenges — given that *in vivo* biomedical imaging operates at a millimeter resolution. Across a spectrum of non-invasive imaging techniques, including recent advancements in ionizing radiation [30], super-resolution ultrasound [31, 32] and MRI [33], diffusion MRI (dMRI) is uniquely sensitive to nominally invisible tissue microgeometry at the scale of the water diffusion length $\ell \sim 1–10 \mu\text{m}$, 2–3 orders of magnitude below the millimeter-size imaging voxels [34–37]. The diffusion length $\ell(t) \equiv$

$\langle x^2(t) \rangle^{1/2}$ is the root mean square displacement of water molecules, which carry nuclear spins detectable via MRI; at typical diffusion times $t \sim 1–100$ ms, it is commensurate with dimensions of cells and organelles, offering an exciting prospect for non-invasive *in vivo* histology at the most relevant biological scale [38–40]. Realizing the ultimate diagnostic potential of biomedical imaging hinges on our ability to interpret macroscopic measurements in terms of specific features of tissue microgeometry. This interpretation fundamentally relies on biophysical modeling [37, 41, 42] to identify the few relevant degrees of freedom that survive massive averaging of local tissue microenvironments of the size $\sim \ell(t)$ within a macroscopic voxel.

Here, we identify the morphological parameters associated with pathological changes in axons that can be probed with dMRI measurements — thereby establishing the link between cellular-level pathology and non-invasive imaging. Specifically, we analytically connect the axonal microgeometry (Fig. 1) to the time-dependent along-tract diffusion coefficient (Fig. 2)

$$D(t) \equiv \frac{\ell^2(t)}{2t} \simeq D_\infty + \frac{c_D}{\sqrt{t}}, \quad t \gg t_c. \quad (1)$$

$D(t)$ is accessible with dMRI [45–50] as the along-tract diffusion coefficient in the clinically feasible regime of diffusion time t exceeding the correlation time $t_c \sim 1$ ms to diffuse past μm -scale axon heterogeneities.

By developing the scattering framework for diffusion in a tube with varying cross-sectional area $A(x)$ along its length x (cf. *Methods* section), we derive Eq. (1) and find exact expressions for its parameters D_∞ and c_D in terms of the relative axon cross-section $\alpha(x)$ (Fig. 2a):

$$\frac{D_0}{D_\infty} = \left\langle \frac{1}{\alpha(x)} \right\rangle, \quad \alpha(x) = \frac{A(x)}{\bar{A}}, \quad (2)$$

* Corresponding author: ali.abdollahzadeh@nyulangone.org

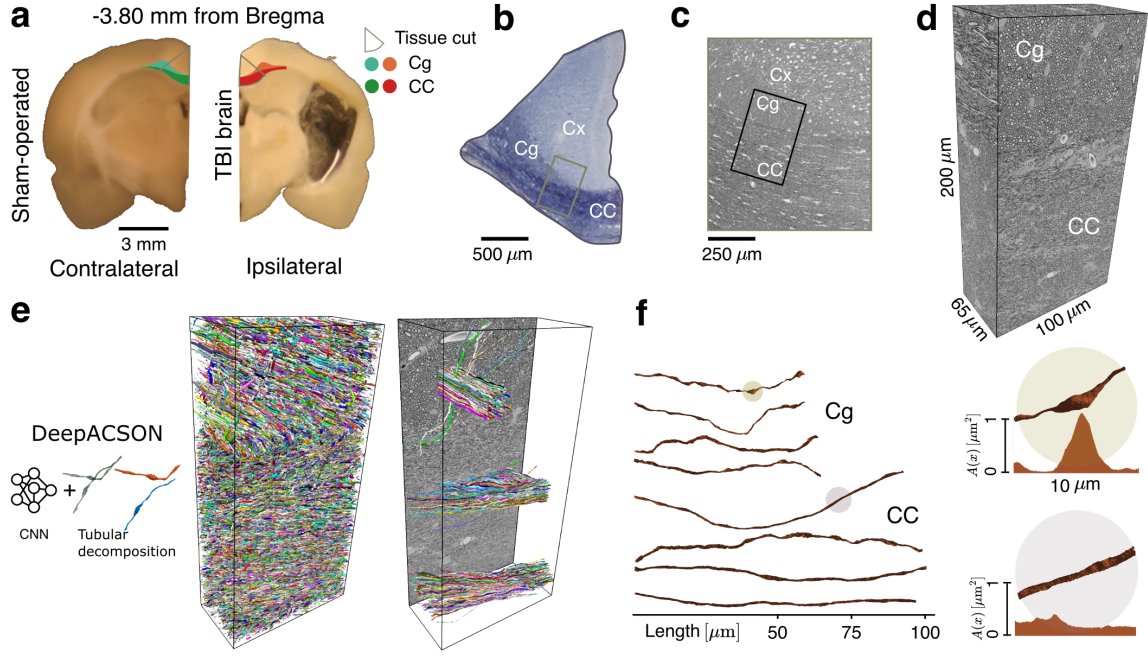


FIG. 1. Axon segmentation and morphology. (a) Representative photomicrographs of 1 mm thick coronal sections, with the cingulum (Cg) and corpus callosum (CC) highlighted. Selected sections for staining encompass parts of the CC, Cg, and cerebral cortex (Cx). (b) A photomicrograph of a semithin section stained with toluidine blue, with a block trimmed further for the serial block-face scanning electron microscopy [43] (SBEM) technique. (c) A low-resolution EM image to navigate for the final SBEM imaging. (d) A representative SBEM volume, voxel size $50 \times 50 \times 50 \text{ nm}^3$, from a large field-of-view $200 \times 100 \times 65 \text{ } \mu\text{m}^3$ that retains two-thirds CC and one-third Cg. (e) DeepACSON [16, 44], a convolutional neural network (CNN)-based technique (see *Methods*) segmented tens of thousands of myelinated axons in each SBEM volume; we sampled and visualized myelinated axons at three random positions. (f) Micrometer-scale along-axon shape variations of representative myelinated axons from Cg and CC. Two $10 \text{ } \mu\text{m}$ -fragments of axons within the shaded circles are zoomed in: the corresponding cross-sectional areas $A(x)$ show a substantial variation (e.g., beading) in one axon and a relative uniformity in the other one.

where $\bar{A} = \langle A(x) \rangle$ is the mean cross-section, and

$$c_D = 2\Gamma_0 \sqrt{\frac{D_\infty}{\pi}}. \quad (3)$$

In Eq. (2), D_0 is the intrinsic diffusion coefficient in the axoplasm, and the geometry-induced attenuation of the diffusion coefficient D_0/D_∞ (the tortuosity factor) is given by the reciprocal relative cross-section averaged along the axon. In Eq. (3), $\Gamma_0 = \Gamma_\eta(q)|_{q \rightarrow 0}$ is the small- q plateau of the power spectral density $\Gamma_\eta(q) = \eta(-q)\eta(q)/L$ (with the dimensions of length), where $\eta(x) = \ln \alpha(x)$, which quantifies long-range cross-sectional fluctuations averaged over axon segments' length $L \sim 100 \text{ } \mu\text{m}$, Fig. 2 (cf. Eq. (19) in *Methods*).

The theory (1)–(3) distills the myriad parameters necessary to specify the geometry of irregular-shaped axons (e.g., those segmented from serial block-face scanning electron microscopy (SBEM) volumes [16, 51, 52]) into just two parameters in Eq. (1): the long-time asymptote D_∞ , and the amplitude c_D of its $t^{-1/2}$ power-law approach. These parameters are further exactly related to the two characteristics of the stochastic axon shape variations $\alpha(x)$ along its coordinate x , Eqs. (2)–(3), thereby bridging the gap between millimeter-level dMRI signal

and micrometer-level changes in axon morphology, expressed in forming beads or varicosities that can occur in response to a variety of pathological conditions and injuries. In what follows, we offer the physical intuition and considerations leading to the above results, validate them using Monte Carlo simulations (Fig. 2), and illustrate our findings in a pathology, chronic TBI, that is particularly subtle to detect with noninvasive imaging (Fig. 3).

Physical picture and the scattering problem

The physical intuition behind the theory (1)–(3) is as follows. Averaging of the reciprocal relative cross-section in Eq. (2) is rationalized via the mapping between diffusivity D_∞ and dc electrical conductivity; an axon is akin to a set of random elementary resistors with resistivities $\sim 1/\alpha(x)$, and resistances in series add up (see *Methods*). The qualitative picture for Eq. (3) involves realizing that an axon, as effectively “seen” by diffusing water molecules, is *coarse-grained* [37, 40, 53] over an increasing diffusion length $\ell(t)$ with time, as illustrated in Fig. 2d: As time progresses, $t_0 < t_1 < t_2 < t_3 < \infty$, molecules sample larger local microenvironments, homogenizing their statistical properties, such that an axon appears increasingly more uniform. This is equivalent to suppressing Fourier harmonics $\eta(q)$ for $q \gtrsim 1/\ell(t)$.

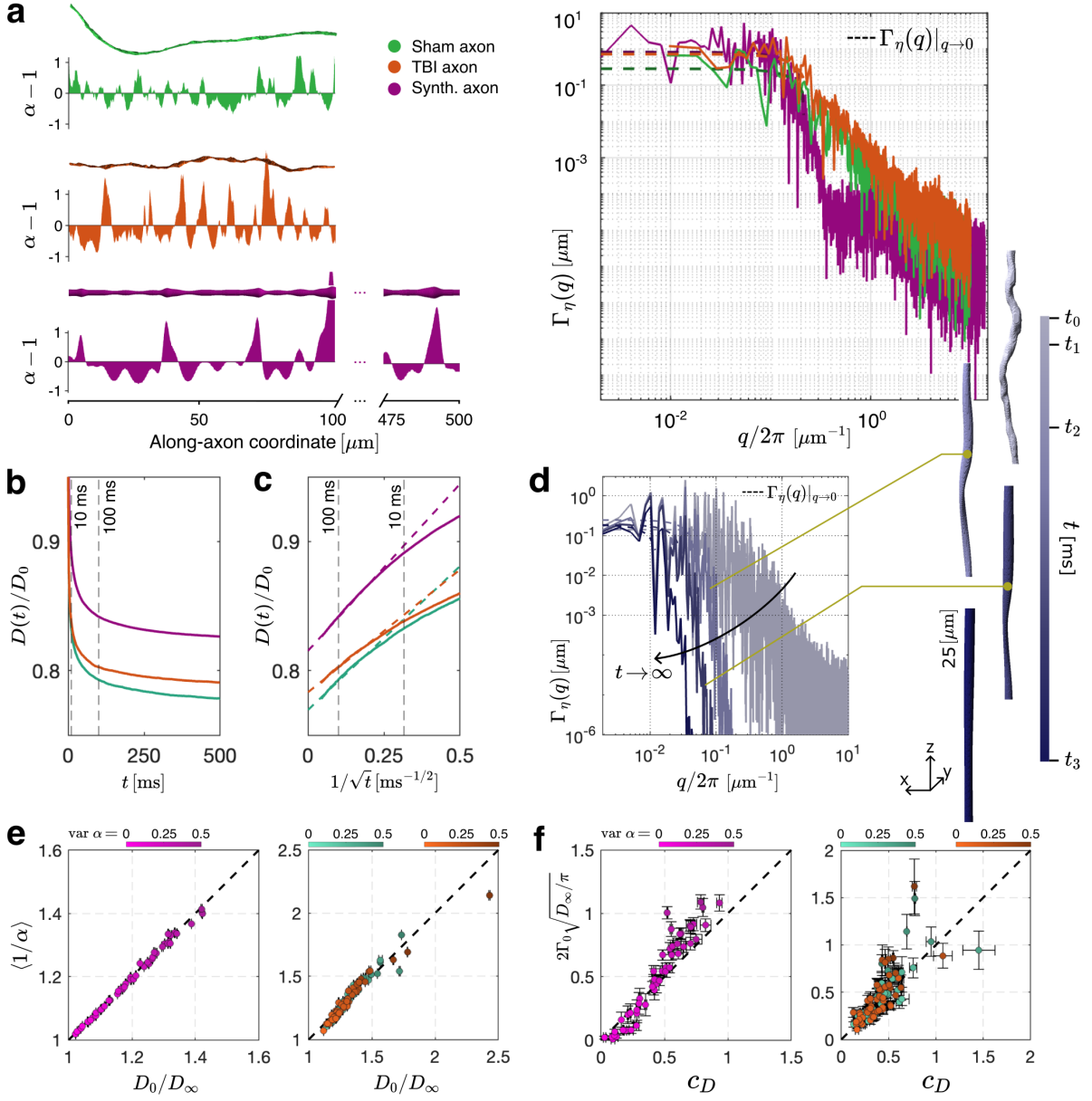


FIG. 2. From axon geometry to along-axon diffusivity. (a) Relative cross-sectional variations α for representative SBEM-segmented myelinated axons (sham and TBI), the synthetic axon, and their power spectral densities $\Gamma_\eta(q)$. Finite plateau $\Gamma_0 = \Gamma_\eta(q)|_{q \rightarrow 0} > 0$ signifies short-range disorder (finite correlation length) in the cross-sections. (b) Monte Carlo simulated $D(t)$ ensemble-averaged over 50 randomly synthesized, 43 randomly sampled SBEM myelinated sham and 57 TBI axons, with colors corresponding to (a). (c) $D(t)$ for all three cases scales asymptotically linearly with $1/\sqrt{t}$, validating Eq. (1). (d) Coarse-graining over the increasing diffusion length $\ell(t)$ makes an axon appear increasingly more uniform, suppressing shape fluctuations $\Gamma_\eta(q)$ with $q \gtrsim 1/\ell(t)$, such that only the $q \rightarrow 0$ plateau Γ_0 “survives” for long t and governs the diffusive dynamics (1). To illustrate the effect, an axon segment is Gaussian-filtered with the standard deviation $\ell(t_i)/\sqrt{2}$ for $\ell(t_i) = 0, 5, 10, 20 \mu\text{m}$. (e) Exact tortuosity limit (2) is validated for both synthetic and SBEM individual axons. Axons with larger cross-sectional variations $\text{var } \alpha$ have higher tortuosity. Horizontal error bars reflect errors in estimating D_∞ from Eq. (1). (f) Predicted c_D , Eq. (3), validated against its MC counterpart estimated from Eq. (1), for individual synthetic and TBI axons (colors as in (a)). Coefficient c_D is larger for axons with greater cross-sectional variations. Error bars reflect errors in estimating c_D from MC-simulated $D(t)$ (horizontal) and estimating the plateau Γ_0 from $\Gamma_\eta(q)$ (vertical), as shown by dashed lines in panel (a).

Hence, it is only the $q \rightarrow 0$ plateau Γ_0 of the power spectral density that “survives” for arbitrarily long t and governs the asymptotic dynamics (1) (provided that the disorder in $\alpha(x)$ is short-ranged, which directly follows from finite Γ_0 , Fig. 2a).

The scattering problem is solved in *Methods* in three steps: (i) coarse-graining of the 3d diffusion equation in a random tube across the cross-section to obtain the one-dimensional (1d) Fick-Jacobs (FJ) equation [54]

$$\partial_t \psi(t, x) = D_0 \partial_x \left(A(x) \partial_x \frac{\psi(t, x)}{A(x)} \right) \quad (4)$$

with arbitrary stochastic $A(x)$, valid for times t exceeding the time to traverse the cross-section ($t \gtrsim 1$ ms); (ii) finding the fundamental solution (Green’s function) of Eq. (4) for a particular configuration of $A(x)$; and (iii) disorder-averaging over the distribution of $A(x)$. Step (iii) gives rise to the translation-invariant Green’s function $G(\omega, q) = 1/[-i\omega + D_\infty q^2 - \Sigma(\omega, q)]$ in the Fourier domain of frequency ω and wavevector q . Steps (ii) and (iii) are fulfilled by summing Feynman diagrams (Fig. 4) representing individual “scattering events” off the cross-sectional variations $\ln \alpha(x)$, which after coarse-graining over sufficiently long $\ell(t)$ become small to yield the self-energy part $\Sigma(\omega, q)$ asymptotically exact in the limit $\omega, q \rightarrow 0$ with $D_\infty q^2/\omega \rightarrow 0$. The dispersive diffusivity [37, 45] $\mathcal{D}(\omega) \simeq D_\infty + \frac{\sqrt{\pi}}{2} c_D \sqrt{-i\omega}$ follows from the pole of $G(\omega, q)$ upon expanding $\Sigma(\omega, q)$ up to q^2 , yielding Eq. (1) via effective medium theory [53, 55]. In *Methods*, we also derive the power law tails $\omega^\vartheta \sim t^{-\vartheta}$ of diffusive metrics for other universality classes of structural fluctuations $\Gamma_\eta(q) \sim |q|^p$, relating the structural exponent α to the FJ dynamical exponent $\vartheta = (p+1)/2$, with $p=0$ (short-range disorder) relevant for the axons.

Undulations [56] (wave-like variations of axon skeleton) cause a slower, $\sim 1/t$ tail [57] in $D(t)$, a sub-leading correction to Eq. (1). In Eq. (25) of *Methods*, we argue that their net effect is the renormalization of $D(t)$ by $1/\xi^2$, where the sinuosity $\xi \geq 1$ is the ratio of the arc to Euclidean length ($\xi - 1 \sim 0.01 - 0.05$, Supplementary Fig. S8 and Eq. (S22)). All subsequent analysis implies the statistics of cross-sectional variations along the arc-length (see *Methods*), with subsequent rescaling by $1/\xi^2$.

Validation in axons segmented from volume EM

We now consider the case of chronic TBI (five months post-injury) [16, 58, 59] both to validate the above theory in a realistic setting and to show how it helps quantify axon morphology changes due to injury. Severe TBI was induced in three rats, and two rats were sham-operated (see *Methods*); animals were sacrificed, and SBEM was performed five months after the sham or TBI procedure. The SBEM datasets were acquired from big tissue volumes of $200 \times 100 \times 65 \mu\text{m}^3$, with 2/3 of each volume corresponding to the corpus callosum and 1/3 to the cingulum. Samples were collected ipsi- and contralaterally (Supplementary Table S1). We applied the DeepACSON

pipeline [16] that combines convolutional neural networks and a tailored tubular decomposition technique [44] to segment the large field-of-view SBEM datasets (Fig. 1). Considering the clinically feasible, long diffusion time asymptote (1), we focus on sufficiently long axons: myelinated axons from the cingulum with a length $L \geq 40 \mu\text{m}$, and from the corpus callosum with $L \geq 70 \mu\text{m}$, yielding a total of $N = 36,363$ myelinated axons.

To validate the theory, Eqs. (1)–(3), we performed Monte Carlo (MC) simulations using the realistic microstructure simulator (RMS) package [60] in 100 SBEM-segmented axons (43 myelinated axons randomly sampled from two sham-operated rats and 57 from three TBI rats), cf. Fig. 2 and *Methods*. As the sample size limits the lengths of SBEM axons, we also created 50 $L = 500 \mu\text{m}$ -long synthetic axons with statistics of $A(x)$ similar to that in SBEM-segmented axons (see *Methods*) to access smaller Fourier harmonics q for reducing errors in estimating Γ_0 . MC-simulated along-axon diffusion coefficients $D_i(t)$ in the i -th axon were volume-weighted (corresponding to spins’ contributions to the dMRI signal) to produce the ensemble-averaged $D(t) = \sum w_i D_i(t)$ for each of the synthetic, sham-operated, and TBI populations, where weights w_i are proportional to axon volumes, $w_i \propto A_i L_i$, and add up to $\sum_i w_i \equiv 1$, Fig. 2b. The asymptotic form, Eq. (1), becomes evident by replotting $D(t)$ as function of $1/\sqrt{t}$, Fig. 2c. The individual $D_i(t)$ also exhibits this scaling, albeit with larger MC noise.

Having validated the functional form (1), we used it to estimate and validate $D_{\infty,i}$ and $c_{D,i}$ for individual axons. For that, we employed linear regression with respect to $1/\sqrt{t}$ for t between 10 and 500 ms. Figure 2e validates Eq. (2) for individual axons. Nearly no deviations occur from the identity line for both synthetic and SBEM-segmented axons, indicating the accuracy and robustness in predicting D_∞ , given the axonal cross-section $A(x)$.

To validate Eq. (3), we calculated the theoretical value of c_D by estimating the plateau Γ_0 of the power-spectral density $\Gamma_\eta(q)$ for individual synthetic and SBEM-segmented axons, as shown in Fig. 2a, 2d, and Supplementary Fig. S1. We then confirmed the agreement between $c_{D,i}$ from MC-simulated $D_i(t)$ for individual axons and their theoretical prediction (3), Fig. 2f, where data points align with the identity line, indicating the absence of bias in the prediction. Random errors in these plots come from errors in estimating Γ_0 , especially for short (SBEM-segmented) axons, as well as from estimating the slope c_D in asymptotic dependence (1) due to MC noise. The numerical agreement with Eq. (3) is notably better for longer synthetic axons. Figure 2f also indicates that as the cross-sectional variation $\text{var}[\alpha(x)]$ increases, the deviations from the identity line become more pronounced, which could be attributed to corrections to FJ equation (4), when the “fast” transverse and “slow” longitudinal dynamics are not fully decoupled.

The validated theory opens up the way to massively speed up predictions of clinically feasible dMRI measurements and their change in pathology: What would nor-

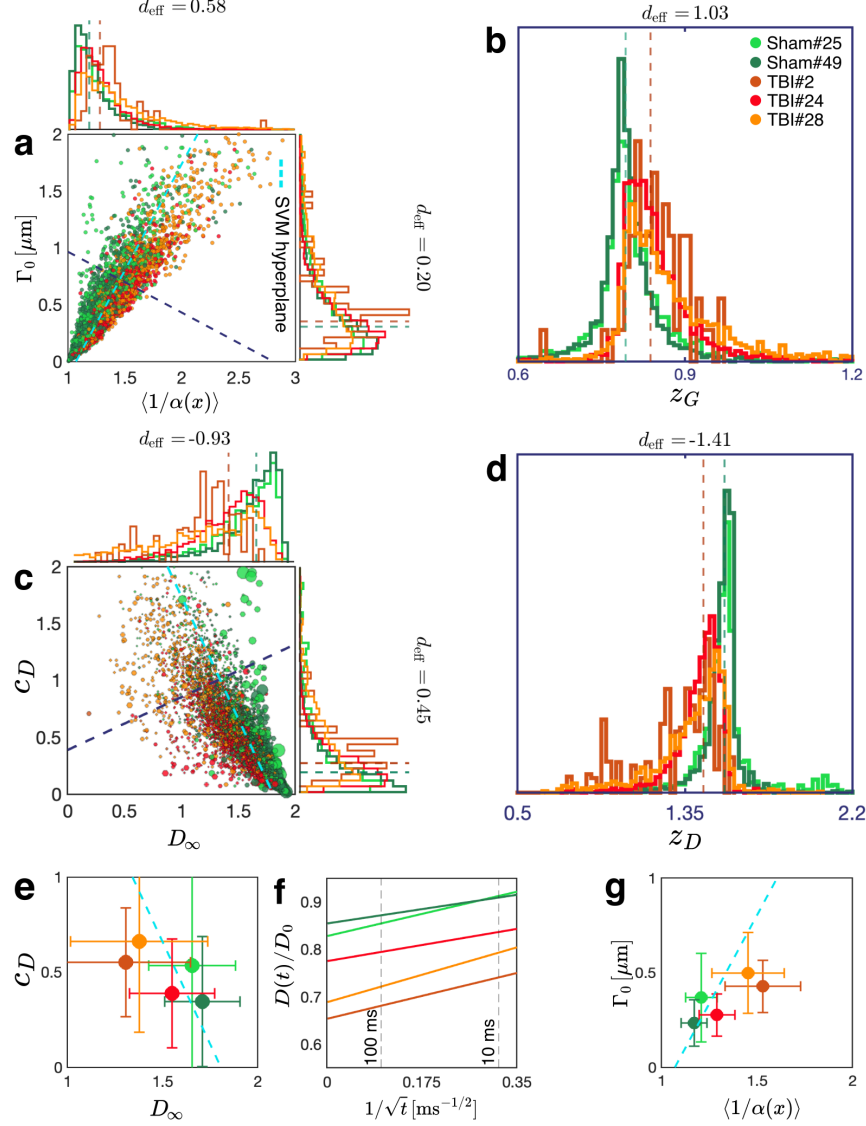


FIG. 3. Effect of chronic TBI on axon morphology and $D(t)$. (a) Geometric tortuosity $\langle 1/\alpha \rangle$, Eq. (2), and the variance Γ_0 of long-range cross-sectional fluctuations entering Eq. (3), are plotted for myelinated axons segmented from the ipsilateral cingulum of sham-operated (shades of green; $N = 3,999$) and TBI (shades of red; $N = 3,999$) rats. (b) The optimal linear combination z_G of the morphological parameters is derived from a trained support vector machine (SVM). Projecting the points onto the dark blue dashed line in (a) perpendicular to the SVM hyperplane constitutes the maximal separation between the two groups. (c) Predicted individual axon diffusion parameters $D_{\infty,i}$ and $c_{D,i}$ from Eqs. (2)–(3) plotted for myelinated axons in (a). The size of each point reflects its weight w_i in the net dMRI-accessible $D(t)$, proportional to the axon volume. (d) The optimal SVM-based linear combination z_D of the diffusion parameters is derived by projecting the points onto the dark blue dashed line in (c) perpendicular to the corresponding SVM hyperplane. The dashed lines overlaid on the distributions in (a–d) represent the medians of the pool of two sham-operated datasets and of the pool of three TBI datasets. (e) The macroscopic diffusivity parameters c_D and D_∞ for each animal are obtained by volume-weighting the individual axonal contributions $D_{\infty,i}$ and $c_{D,i}$. The SVM hyperplane (cyan dashed line) is the same as that for the diffusion parameters of individual axons in (c). (f) Predicting the along-tract $D(t)/D_0$ as a function of $1/\sqrt{t}$, Eq. (1), based on the overall D_∞ and c_D in (e). (g) The effect of TBI on the ensemble-averaged geometry is illustrated by transforming the macroscopic ensemble diffusivity in (e,f), as if from an MRI measurement, back onto the space of morphological parameters $\langle 1/\alpha \rangle$ and Γ_0 , via inverting Eqs. (2)–(3). The SVM hyperplane (cyan dashed line) is the same as that for the morphological parameters of individual axons in (a). Error bars correspond to standard deviations of $\langle 1/\alpha \rangle$ and Γ_0 , based on errors in measuring the volume-weighted D_∞ and c_D in (e).

mally require over a year of GPU-powered MC simulations in the realistic microstructure of Fig. 1 for tens of thousands of segmented axons is now predicted in mere seconds on a regular desktop computer by calculating the relevant dMRI parameters using Eqs. (2) and (3) based on axon cross-sections $A(x)$.

Effects of TBI on axon morphology and diffusion

In Fig. 3, we examine the effects of injury in both the morphological coordinates ($\langle 1/\alpha \rangle$ and Γ_0) and the diffusion coordinates (D_∞ and c_D). These equivalent sets of neuronal damage markers are related via Eqs. (2)–(3).

Morphological parameters of the individual axons are shown in Fig. 3a for the ipsilateral cingulum (cf. Supplementary Figs. S2–S4 for other regions). TBI causes an increase in both $\langle 1/\alpha \rangle$ and Γ_0 and manifests itself as a substantial change (1 standard deviation) of their optimal support vector machine (SVM) combination z_G (subscript G denotes geometry), Fig. 3b. The geometric parameter z_G shows small variations within sham and TBI groups and a larger difference between the groups.

Diffusional parameters of the axons, D_∞ and c_D , both decrease in TBI (Fig. 3c). Their optimal SVM combination z_D (subscript D stands for diffusion) shows an even larger, 1.4 standard deviation change in TBI, Fig. 3d. Note that the individual D_∞ and c_D are rescaled by the corresponding sinuosity, Supplementary Eq. (S22). As Supplementary Fig. S8 shows, sinuosity increases in TBI.

Due to large sample sizes in panels a and c, we avoid traditional hypothesis testing, which is prone to type I errors. Hence, we use a nonparametric measure d_{eff} of the effect size, defined as the difference between the medians normalized by the pooled median absolute deviation (Eq. (26) in *Methods*).

The along-tract ensemble diffusivity (1) with volume-weighted $D_\infty = \sum_i w_i D_{\infty,i}$ and $c_D = \sum_i w_i c_{D,i}$, shown in Fig. 3e–f, is predicted based on $D(t)$ originating from five distinct voxels in five animals with aligned impermeable myelinated axons. The same SVM hyperplane that separates volume-weighted diffusional parameters of individual axons in Fig. 3c can also separate their ensemble diffusivity. Plugging the c_D and D_∞ values into Eq. (1), we predict the associated $D(t)$ for these five voxels as a function of $1/\sqrt{t}$ in Fig. 3d. This representation mimics a dMRI measurement, demonstrating how MRI can capture TBI-related geometric changes in each voxel.

Finally, we invert Eqs. (2)–(3) to interpret the ensemble-averaged $D(t)$ in terms of the ensemble-averaged morphological coordinates. The separability between the groups is clearly manifest: interestingly, the five points in Fig. 3g, derived from inverting the volume-weighted diffusion parameters in Fig. 3e, are still separable by the same SVM hyperplane that distinguishes the geometrical parameters of individual axons in Fig. 3a.

Based on Fig. 3, we make two observations. (i) The volume-weighting of individual axon contributions in the dMRI-accessible $D(t)$, Fig. 3c, *magnifies* the TBI effect size as compared to the morphological analysis (Fig. 3a).

This can be rationalized by noting that TBI preferentially reduces the radii of thicker axons (Supplementary Fig. S5, top row). Hence, the weights w_i change in TBI to emphasize thinner axons, which tend to have greater cross-sectional variations (hence, lower D_∞ and higher c_D). (ii) While $\langle 1/\alpha \rangle$ exhibits higher sensitivity than Γ_0 , it is the *two-dimensional* parameter space derived from the time-dependent diffusion (1) that yields the largest effect size for the optimal pathology marker z_G or z_D .

Geometric interpretation of axonal degeneration

We first consider the tortuosity (2), which is always above 1; its excess $\langle 1/\alpha \rangle - 1 = \text{var } \alpha + \mathcal{O}(\langle \delta \alpha^3 \rangle)$ is dominated by the variance $\text{var } \alpha$ of relative axon cross-sections. This can be seen by expanding the geometric series $1/(1 + \delta \alpha)$ in the deviation $\delta \alpha = \alpha - 1$, and averaging term-by-term, with $\langle \delta \alpha \rangle \equiv 0$. Indeed, in Fig. 2e, axons with larger cross-sectional variations $\text{var } \alpha$ have larger tortuosity.

The meaning of the power spectral density plateau Γ_0 can be understood from a *single-bead model*. Consider the relative cross-sectional area $\alpha(x) = e^{\eta(x)}$, with $\eta(x) = \eta_0 + \sum_m \eta_1(x - x_m)$, as coming from a set of identical “multiplicative” beads with shape $\eta_1(x)$, placed at random positions x_m on top of the constant η_0 . In Supplementary Eq. (S13), for this model we find $\Gamma_0 = (\sigma_a^2/\bar{a}) \phi^2$, where \bar{a} and σ_a are the mean and standard deviation of the intervals between the positions of successive beads (assuming uncorrelated intervals), and $\phi = \int dx \eta_1(x)/\bar{a}$ is a dimensionless “bead fraction”. The factor σ_a^2/\bar{a} in Γ_0 quantifies the disorder in the bead positions, while ϕ^2 quantifies the prominence of the beads. Hence, Γ_0 decreases when placing the same beads more regularly and increases for more pronounced beads.

Analyzing the origins of Γ_0 according to the single-bead model in Supplementary Figs. S6–S7, we found that TBI changes the statistics of bead positions, with (i) a decrease in the mean distance \bar{a} between beads, meaning the number of beads per unit length increases, which is in line with the formation of beads [14, 15]; and (ii) a decrease in the standard deviation σ_a of the bead intervals, i.e., beads become effectively more ordered (Supplementary Fig. S7). Note that the decrease in σ_a^2 is stronger than the decrease in \bar{a} , such that the overall factor σ_a^2/\bar{a} decreases. TBI also caused a decrease in ϕ^2 .

Discussion and outlook

From the neurobiological perspective, the mechanical forces inflict damage on axons during the immediate injury and trigger a cascade of detrimental effects such as swelling, disconnection, degeneration, or regeneration over time [15]. In particular, swellings, resulting from interruptions and accumulations in axonal transport, often follow an approximately regular arrangement akin to “beads on a string,” defining a pathological phenotype known as axonal varicosities [14, 61, 62]. These phenomena can persist for months or even years post-injury [59, 63].

Our approach shows that axons that survived the immediate impact of injury exhibit morphological alter-

ations in the chronic phase. While not immediately obvious to the naked eye, our proposed morphological and diffusional parameters remain remarkably sensitive to neuronal injury. The repercussions of the laterally induced brain injury affected both the cingulum and corpus callosum, with a pronounced effect on the cingulum. This can be attributed to our observation of higher directional homogeneity in axons within the cingulum, rendering a bundle with more uniform statistical properties than the corpus callosum. Furthermore, the response to injury remained localized and confined to the ipsilateral side, closer to the injury site. The contralateral hemisphere, distant from the immediate impact, exhibits only marginal effects, as expected. Detecting such subtle changes in morphology is crucial as they can contribute to axonal dysfunction, such as altered conduction velocity observed in animal models [64–66], which further may be linked to a diverse array of physical and cognitive outcomes, as well as neurodegenerative conditions, including Alzheimer’s disease [67] and epilepsy [68].

Accessing the along-tract diffusion coefficient $D(t)$ corresponds to a clinically feasible, lowest-order $\sim q^2$ dMRI weighting, as opposed to very strong diffusion gradients (available on only a few custom-made scanners) required for mapping axon radii [69]. Moreover, in Supplementary Eq. (S7), we show that the tortuosity $\langle 1/\alpha \rangle$ is sensitive to the lower-order moments of axon radius compared to the effective radius r_{eff} measured at very strong gradients [69]. Hence, the tortuosity better characterizes the bulk of the distribution, while r_{eff} is dominated by its tail, Supplementary Fig. S5 and Eq. (S2). Practically, $D(t)$ can be accessed via intracellular metabolites using diffusion-weighted spectroscopy [47], as well as with water diffusion using pulsed gradients [46, 50], or oscillating gradients [45, 48, 49] measuring the real part of the dispersive $\mathcal{D}(\omega)$ [37, 53]. For water dMRI, we expect the along-axon extra-axonal space contribution to be similar given that its geometric profile mirrors that of intra-axonal space, yet with notably smaller volume fraction [70] further suppressed by the relatively faster T_2 relaxation [71–73]. The $t^{-1/2}$ power law tail in Eq. (1) is similar to that found for one-dimensional short-range disorder in local stochastic diffusion coefficient $D(x)$ of the heterogeneous diffusion equation [53], yet it comes from a distinctly different dynamical equation (4). Such a slow power-law tail dominates the faster-decaying, $\sim 1/t$ contributions due to confined geometries [34], undulations [56, 57], or structural disorder in higher spatial dimensions [53], and thus can be used to identify the contribution from effectively one-dimensional structurally-disordered neuronal processes.

As an outlook, the present approach combines the unique strengths of machine learning (neural networks for segmentation of large SBEM datasets) and theoretical physics (identifying relevant degrees of freedom) to uncover the information content of diagnostic imaging orders of magnitude below the resolution. An exact asymptotic solution of a key dynamical equation rad-

ically reduces the dimensionality of the problem: just two geometric parameters not immediately obvious and apparent — average reciprocal cross-sectional area and the variance of long-range cross-sectional fluctuations — embody the specificity of a bulk MRI measurement to changes of axon microstructure in TBI, and enable a near-instantaneous prediction of a dMRI measurement from tens of thousands of axons. The two parameters are sensitive to the variation of the cross-sectional area and the statistics of bead positions, opening a non-invasive window into axon shape alterations. This approach can be used to detect previously established μm -scale changes that occur not only in axons but also in the morphology of dendrites during aging [74, 75], and pathologies such as stroke [76], Alzheimer’s [77] and Parkinson’s [78, 79] diseases, with an overarching aim of turning MRI into a non-invasive *in vivo* tissue microscope.

Acknowledgements

The research was supported by the NIH under awards R01 NS088040 and R21 NS081230, the Irma T. Hirsch fund. A.A. was funded by the Academy of Finland (grant #360360). The research was performed at the Center of Advanced Imaging Innovation and Research (CAI2R, www.cai2r.net), a Biomedical Technology Resource Center supported by NIBIB with the award P41 EB017183. A.S. was funded by the Academy of Finland (grant #323385) and the Erkko Foundation. H.H.L. was supported by the Office of the Director and NIDCR of NIH with the award DP5 OD031854.

Author contributions

A.A., E.F., and D.S.N. conceived the project and designed the study. A.A. conducted electron microscopy image analysis, performed Monte Carlo simulations, and analyzed the data. D.S.N. developed theory. R.C.-L. and H.-H.L. contributed to MC simulations. A.S. provided animal models and EM imaging. A.A. and D.S.N. wrote the manuscript. E.F. and D.S.N. supervised the project. All authors commented on and approved the final manuscript.

Competing interests

The authors declare no competing financial interests.

Data availability

All data that support the findings are available from the corresponding author upon request.

Code availability

The source codes of DeepACSON software are publicly available at <https://github.com/aAbdz/DeepACSON>. The source codes of the Monte Carlo simulator (the RMS package) are publicly available at <https://github.com/NYU-DiffusionMRI>.

- [1] V. L. Feigin, T. Vos, E. Nichols, M. O. Owolabi, W. M. Carroll, M. Dichgans, G. Deuschl, P. Parmar, M. Brainin, and C. Murray, *The Lancet Neurology* **19**, 255 (2020), publisher: Elsevier.
- [2] T. Ohgami, T. Kitamoto, and J. Tateishi, *Neuroscience Letters* **136**, 75 (1992).
- [3] G. B. Stokin, C. Lillo, T. L. Falzone, R. G. Brusch, E. Rockenstein, S. L. Mount, R. Raman, P. Davies, E. Masliah, D. S. Williams, and L. S. B. Goldstein, *Science* **307**, 1282 (2005).
- [4] J. S. Kim-Han, J. A. Antenor-Dorsey, and K. L. O'Malley, *The Journal of Neuroscience* **31**, 7212 (2011).
- [5] M. P. Coleman, *Experimental Neurology* **246**, 1 (2013).
- [6] G. Szebenyi, G. A. Morfini, A. Babcock, M. Gould, K. Selkoe, D. L. Stenoi, M. Young, P. W. Faber, M. E. MacDonald, M. J. McPhaul, and S. T. Brady, *Neuron* **40**, 41 (2003).
- [7] W.-C. M. Lee, M. Yoshihara, and J. T. Littleton, *Proceedings of the National Academy of Sciences* **101**, 3224 (2004).
- [8] B. D. Trapp, J. Peterson, R. M. Ransohoff, R. Rudick, S. Mörk, and L. Bö, *New England Journal of Medicine* **338**, 278 (1998).
- [9] I. Nikić, D. Merkler, C. Sorbara, M. Brinkoetter, M. Kreutzfeldt, F. M. Bareyre, W. Brück, D. Bishop, T. Misgeld, and M. Kerschensteiner, *Nature Medicine* **17**, 495 (2011).
- [10] E. T. Wood, I. Ronen, A. Techawiboonwong, C. K. Jones, P. B. Barker, P. Calabresi, D. Harrison, and D. S. Reich, *The Journal of Neuroscience* **32**, 6665 (2012).
- [11] P. Li and T. H. Murphy, *J Neurosci* **28**, 11970 (2008).
- [12] M. D. Budde and J. A. Frank, *Proceedings of the National Academy of Sciences* **107**, 14472 (2010).
- [13] E. G. Sozmen, A. Kolekar, L. A. Havton, and S. T. Carmichael, *Journal of Neuroscience Methods* **180**, 261 (2009).
- [14] M. D. Tang-Schomer, V. E. Johnson, P. W. Baas, W. Stewart, and D. H. Smith, *Experimental Neurology* **233**, 364 (2012).
- [15] C. S. Hill, M. P. Coleman, and D. K. Menon, *Trends in Neurosciences* **39**, 311 (2016).
- [16] A. Abdollahzadeh, I. Belevich, E. Jokitalo, A. Sierra, and J. Tohka, *Communications Biology* **4**, 179 (2021).
- [17] G. M. G. Shepherd, M. Raastad, and P. Andersen, *Proceedings of the National Academy of Sciences* **99**, 6340 (2002).
- [18] C. Gu, *Frontiers in Molecular Neuroscience* **14**, 10.3389/fnmol.2021.610857 (2021).
- [19] C. Geula, N. Nagykeri, A. Nicholas, and C.-K. Wu, *Journal of Neuropathology & Experimental Neurology* **67**, 309 (2008).
- [20] M. Marangoni, R. Adalbert, L. Janeckova, J. Patrick, J. Kohli, M. P. Coleman, and L. Conforti, *Neurobiology of Aging* **35**, 2382 (2014).
- [21] E. Chevalier-Larsen and E. L. Holzbaur, *Biochimica et Biophysica Acta (BBA) - Molecular Basis of Disease* **1762**, 1094 (2006).
- [22] S. Millecamps and J.-P. Julien, *Nature Reviews Neuroscience* **14**, 161 (2013).
- [23] J. N. Sleight, A. M. Rossor, A. D. Fellows, A. P. Tosolini, and G. Schiavo, *Nature Reviews Neurology* **15**, 691 (2019).
- [24] S. H. Berth and T. E. Lloyd, *Journal of Clinical Investigation* **133**, 10.1172/JCI168554 (2023).
- [25] M. Coleman, *Nature Reviews Neuroscience* **6**, 889 (2005).
- [26] L. R. Fischer, D. G. Culver, P. Tennant, A. A. Davis, M. Wang, A. Castellano-Sanchez, J. Khan, M. A. Polak, and J. D. Glass, *Experimental Neurology* **185**, 232 (2004).
- [27] S. Roy, B. Zhang, V. M.-Y. Lee, and J. Q. Trojanowski, *Acta Neuropathologica* **109**, 5 (2005).
- [28] H. Takeuchi, T. Mizuno, G. Zhang, J. Wang, J. Kawanokuchi, R. Kuno, and A. Suzumura, *Journal of Biological Chemistry* **280**, 10444 (2005).
- [29] A. Datar, J. Ameeramja, A. Bhat, R. Srivastava, A. Mishra, R. Bernal, J. Prost, A. Callan-Jones, and P. A. Pullarkat, *Biophysical Journal* **117**, 880 (2019).
- [30] K. Rajendran, M. Petersilka, A. Henning, E. R. Shanblatt, B. Schmidt, T. G. Flohr, A. Ferrero, F. Baffour, F. E. Diehn, L. Yu, P. Rajiah, J. G. Fletcher, S. Leng, and C. H. McCollough, *Radiology* **303**, 130 (2022).
- [31] C. Errico, J. Pierre, S. Pezet, Y. Desailly, Z. Lenkei, O. Couture, and M. Tanter, *Nature* **527**, 499 (2015).
- [32] B. Heiles, A. Chavignon, V. Hingot, P. Lopez, E. Teston, and O. Couture, *Nature Biomedical Engineering* **6**, 605 (2022).
- [33] N. Seiberlich, V. Gulani, A. Campbell-Washburn, S. Sourbron, M. I. Doneva, F. Calamante, and H. H. Hu, eds., *Quantitative Magnetic Resonance Imaging*, 1st ed., Vol. 1 (Elsevier, 2020).
- [34] D. S. Grebenkov, *Rev. Mod. Phys.* **79**, 1077 (2007).
- [35] D. K. Jones, *Diffusion MRI: Theory, Methods, and Applications* (Oxford University Press, 2010).
- [36] V. G. Kiselev, *NMR in Biomedicine* **30**, e3602 (2017).
- [37] D. S. Novikov, E. Fieremans, S. N. Jespersen, and V. G. Kiselev, *NMR in Biomedicine* **32**, e3998 (2019).
- [38] N. Weiskopf, L. J. Edwards, G. Helms, S. Mohammadi, and E. Kirilina, *Nature Reviews Physics* **3**, 570 (2021).
- [39] V. G. Kiselev, *Journal of Neuroscience Methods* **347**, 108910 (2021).
- [40] D. S. Novikov, *Journal of Neuroscience Methods* **351**, 108947 (2021).
- [41] D. C. Alexander, T. B. Dyrby, M. Nilsson, and H. Zhang, *NMR in Biomedicine* **32**, e3841 (2019).
- [42] D. S. Novikov, V. G. Kiselev, and S. N. Jespersen, *Magnetic Resonance in Medicine* **79**, 3172 (2018).
- [43] W. Denk and H. Horstmann, *PLoS Biology* **2**, e329 (2004), iSBN: 1545-7885 (Electronic)\n1544-9173 (Linking).
- [44] A. Abdollahzadeh, A. Sierra, and J. Tohka, *IEEE Access* **9**, 23979 (2021).
- [45] M. D. Does, E. C. Parsons, and J. C. Gore, *Magn Reson Med* **49**, 206 (2003).
- [46] E. Fieremans, L. M. Burcaw, H. H. Lee, G. Lember-skiy, J. Veraart, and D. S. Novikov, *NeuroImage* **129**, 414 (2016).
- [47] M. Palombo, C. Ligneul, C. Najac, J. Le Douce, J. Flament, C. Escartin, P. Hantraye, E. Brouillet, G. Bonvento, and J. Valette, *Proceedings of the National Academy of Sciences* **113**, 201504327 (2016).
- [48] A. Arbabi, J. Kai, A. R. Khan, and C. A. Baron, *Magnetic Resonance in Medicine* **83**, 2197 (2020).

- [49] E. T. Tan, R. Y. Shih, J. Mitra, T. Sprenger, Y. Hua, C. Bhushan, M. A. Bernstein, J. A. McNab, J. K. DeMarco, V. B. Ho, and T. K. Foo, *Magnetic Resonance in Medicine* **84**, 950 (2020).
- [50] H.-H. Lee, A. Papaioannou, S.-L. Kim, D. S. Novikov, and E. Fieremans, *Communications Biology* **3**, 354 (2020).
- [51] A. Abdollahzadeh, I. Belevich, E. Jokitalo, J. Tohka, and A. Sierra, *Scientific Reports* **9**, 6084 (2019).
- [52] H.-H. Lee, K. Yaros, J. Veraart, J. L. Pathan, F.-X. Liang, S. G. Kim, D. S. Novikov, and E. Fieremans, *Brain Structure and Function* **224**, 1469 (2019).
- [53] D. S. Novikov, J. H. Jensen, J. A. Helpert, and E. Fieremans, *Proceedings of the National Academy of Sciences* **111**, 5088 (2014).
- [54] R. Zwanzig, *The Journal of Physical Chemistry* **96**, 3926 (1992).
- [55] D. S. Novikov and V. G. Kiselev, *NMR in Biomedicine* **23**, 682 (2010).
- [56] J. Brabec, S. Lasić, and M. Nilsson, *NMR in Biomedicine* **33**, 10.1002/nbm.4187 (2020).
- [57] H.-H. Lee, S. N. Jespersen, E. Fieremans, and D. S. Novikov, *NeuroImage* **223**, 117228 (2020).
- [58] A. Abdollahzadeh, I. Belevich, E. Jokitalo, J. Tohka, and A. Sierra, *Segmentation of white matter ultrastructures in 3D electron microscopy* (2020).
- [59] I. S. M. Molina, R. A. Salo, A. Abdollahzadeh, J. Tohka, O. Gröhn, and A. Sierra, *eNeuro* **7**, 1 (2020).
- [60] H.-H. Lee, E. Fieremans, and D. S. Novikov, *Journal of Neuroscience Methods* **350**, 109018 (2021).
- [61] C. W. Rand and C. B. Courville, *Archives of Neurology & Psychiatry* **55**, 79 (1946).
- [62] P. A. Pullarkat, P. Dommersnes, P. Fernández, J.-F. Joanny, and A. Ott, *Physical Review Letters* **96**, 048104 (2006), arXiv:physics/0603122.
- [63] A. C. Rodriguez-Paez, J. P. Brunschwig, and H. M. Bramlett, *Acta Neuropathologica* **109**, 603 (2005).
- [64] A. Baker, N. Phan, R. Moulton, M. Fehlings, Y. Yucel, M. Zhao, E. Liu, and G. Tian, *Journal of Neurotrauma* **19**, 587 (2002).
- [65] T. M. Reeves, L. L. Phillips, and J. T. Povlishock, *Experimental Neurology* **196**, 126 (2005).
- [66] V. E. Johnson, W. Stewart, and D. H. Smith, *Experimental Neurology* **246**, 35 (2013).
- [67] V. E. Johnson, J. E. Stewart, F. D. Begbie, J. Q. Trojanowski, D. H. Smith, and W. Stewart, *Brain* **136**, 28 (2013).
- [68] A. Pitkänen and R. Immonen, *Neurotherapeutics* **11**, 286 (2014).
- [69] J. Veraart, D. Nunes, U. Rudrapatna, E. Fieremans, D. K. Jones, D. S. Novikov, and N. Shemesh, *eLife* **9**, 10.7554/eLife.49855 (2020).
- [70] E. Syková and C. Nicholson, *Physiol Rev* **88**, 1277 (2008).
- [71] J. Veraart, D. S. Novikov, and E. Fieremans, *NeuroImage* **182**, 360 (2018).
- [72] B. Lampinen, F. Szczepankiewicz, J. Mårtensson, D. van Westen, O. Hansson, C. Westin, and M. Nilsson, *Magnetic Resonance in Medicine* **84**, 1605 (2020).
- [73] C. M. Tax, E. Kleban, M. Chamberland, M. Baraković, U. Rudrapatna, and D. K. Jones, *NeuroImage* **236**, 117967 (2021).
- [74] P. Mukherjee, J. H. Miller, J. S. Shimony, J. V. Philip, D. Nehra, A. Z. Snyder, T. E. Conturo, J. J. Neil, and R. C. McKinstry, *American Journal of Neuroradiology* **23** (2002).
- [75] C.-L. Pan, C.-Y. Peng, C.-H. Chen, and S. McIntire, *Proceedings of the National Academy of Sciences* **108**, 9274 (2011).
- [76] S. Zhang, J. Boyd, K. Delaney, and T. H. Murphy, *J Neurosci* **25**, 5333 (2005).
- [77] M. D. Ikonovic, E. E. Abrahamson, B. A. Isanski, J. Wu, E. J. Mufson, and S. T. DeKosky, *Archives of Neurology* **64**, 1312 (2007).
- [78] Y. Li, W. Liu, T. F. Oo, L. Wang, Y. Tang, V. Jackson-Lewis, C. Zhou, K. Geghman, M. Bogdanov, S. Przedborski, M. F. Beal, R. E. Burke, and C. Li, *Nature Neuroscience* **12**, 826 (2009).
- [79] P. Tagliaferro and R. E. Burke, *Journal of Parkinson's Disease* **6**, 1 (2016).
- [80] I. Kharatishvili, J. P. Nissinen, T. K. McIntosh, and A. Pitkänen, *Neuroscience* **140**, 685 (2006).
- [81] T. Deerinck, E. Bushong, V. Lev-Ram, X. Shu, R. Tsien, and M. Ellisman, *Microscopy and Microanalysis* **16**, 1138 (2010).
- [82] A. Behanova, A. Abdollahzadeh, I. Belevich, E. Jokitalo, A. Sierra, and J. Tohka, *Computer Methods and Programs in Biomedicine* **220**, 106802 (2022).
- [83] I. Belevich, M. Joensuu, D. Kumar, H. Vihinen, and E. Jokitalo, *PLoS Biology* **14**, 1 (2016).
- [84] J. Veraart, E. Fieremans, and D. S. Novikov, *NeuroImage* **185**, 379 (2019).
- [85] B. Altshuler and A. Aronov, in *Electron-Electron Interactions in Disordered Systems*, Vol. 10, edited by A. L. Efros and M. Pollak (Elsevier, Amsterdam, 1985) pp. 1–153.
- [86] J.-P. Bouchaud and A. Georges, *Physics Reports - Review Section of Physics Letters* **195**, 127 (1990).
- [87] S. Torquato, *Physics Reports* **745**, 1 (2018), hyperuniform States of Matter.
- [88] J. L. Hodges Jr. and E. L. Lehmann, *The Annals of Mathematical Statistics* **34**, 598 (1963).
- [89] L. M. Burcaw, E. Fieremans, and D. S. Novikov, *NeuroImage* **114**, 18 (2015).
- [90] Y. Assaf, T. Blumenfeld-Katzir, Y. Yovel, and P. J. Basser, *Magnetic Resonance in Medicine* **59**, 1347 (2008).
- [91] C. H. Neuman, *The Journal of Chemical Physics* **60**, 4508 (1974).

METHODS

Animal model and SBEM imaging

We utilized five adult male Sprague-Dawley rats (Harlan Netherlands B.V., Horst, Netherlands; weighing between 320 and 380 g and aged ten weeks). The rats were individually housed in a controlled environment with a 12-hour light/dark cycle and had unrestricted access to food and water. All animal procedures were approved by the Animal Care and Use Committee of the Provincial Government of Southern Finland and performed according to the European Community Council Directive 86/609/EEC guidelines.

TBI was induced in three rats using the lateral fluid percussion injury method described in ref. [80]. The rats were anesthetized, and a craniectomy with a 5 mm diameter was performed between bregma and lambda on the left convexity. Lateral fluid percussion injury induced a severe injury at the exposed intact dura. Two rats underwent a sham operation that involved all surgical procedures except the impact. After five months following TBI or sham operation, rats were transcardially perfused, and their brains were extracted and post-fixed. Using a vibrating blade microtome, the brains were sectioned into 1-mm thick coronal sections. From each brain, sections located at -3.80 mm from bregma were chosen and further dissected into smaller samples containing the regions of interest. Figure 1a shows a sham-operated rat's contralateral hemisphere and the TBI rat's ipsilateral hemisphere. We collected two samples for each brain: the ipsilateral and contralateral samples, including the cingulum and corpus callosum. The samples were stained following an enhanced protocol with heavy metals [81] (Fig. 1b). After sample selection, the blocks were trimmed into pyramidal shapes, ensuring block stability in the microscope sectioning process (For further animal model and tissue preparation details, see ref. [82]).

The blocks were imaged using the SBEM technique [43] (Quanta 250 Field Emission Gun; FEI Co., Hillsboro, OR, USA, with 3View). For that, each block was positioned with its face in the $x - y$ plane, and the cutting was done in the z direction. Images were consistently captured with the voxel size of $50 \times 50 \times 50 \text{ nm}^3$ from a large field-of-view $200 \times 100 \times 65 \text{ }\mu\text{m}^3$ at a specific location in the white matter of both sham-operated and TBI animals in both hemispheres. We used Microscopy Image Browser [83] (MIB; <http://mib.helsinki.fi>) to align the SBEM images. We aligned the images by measuring the translation between the consecutive SBEM images using the cross-correlation cost function (MIB, Drift Correction). We acquired a series of shift values in x direction and a series of shift values in y direction. The running average of the shift values (window size was 25) was subtracted from each series to preserve the orientation of myelinated axons. We applied contrast normalization such that the mean and standard deviation of the histogram of each image match the mean and standard

deviation of the whole image stack. The volume sizes of the acquired EM datasets are provided in Supplementary Table S1.

Segmentation of myelinated axons

We used the DeepACSON pipeline, a **deep** neural network-based **automatic** segmentation of axons [16] to segment the acquired large field-of-view low-resolution SBEM images. This pipeline addresses the challenges posed by severe membrane discontinuities, which are inescapable with low-resolution imaging of tens of thousands of myelinated axons. It combines the current deep learning-based semantic segmentation methods with a shape decomposition technique [44] to achieve instance segmentation, taking advantage of prior knowledge about axon geometry. The instance segmentation approach in DeepACSON adopts a top-down perspective, i.e., under-segmentation and subsequent split, based on the tubularity of the shape of axons, decomposing under-segmented axons into their individual components.

In our analysis, we only included axons that were longer than $70\text{ }\mu\text{m}$ in the corpus callosum and $40\text{ }\mu\text{m}$ in the cingulum. We further excluded axons with protrusion causing bifurcation in the axonal skeleton and axons with narrow necks with a cross-sectional area smaller than nine voxels for MC simulations.

Synthetic axon generation

To generate axons with randomly positioned beads, the varying area $A(x)$ was calculated by convolving random number density $n(x)$ of restrictions along the line x with a Gaussian kernel of width σ_1 representing a "bead":

$$A(x) = A_0 + n(x) * A_1 \frac{e^{-x^2/2\sigma_1^2}}{\sqrt{2\pi\sigma_1^2}}, \quad (5)$$

where we fixed $A_0 = \pi \cdot (0.5)^2 \text{ }\mu\text{m}^2$, let the bead amplitude A_1 range between $[0.1, 2.5] \text{ }\mu\text{m}^2$, and the bead width σ_1 between $[3, 7] \text{ }\mu\text{m}$. The random bead placement $n(x)$ was generated to have a normally distributed inter-bead distance a with a mean $\bar{a} \equiv 1/\langle n(x) \rangle$ ranging between $[3, 7] \text{ }\mu\text{m}$ and a standard deviation σ_a in the range $[0.8 \cdot \bar{a}, 1.2 \cdot \bar{a}]$. The parameters were set to vary in broader ranges compared to refs. [50, 51] to cover a broader range of potential axonal geometries.

Monte Carlo simulations

Monte Carlo simulations of random walkers were performed using Realistic Monte Carlo Simulations (RMS) package [60] implemented in CUDA C++ for diffusion in a continuous space within the segmented intra-axonal

space geometries as described in ref. [50]. Random walkers explore the geometry of intra-axonal spaces; when a walker encounters cell membranes, the walker is elastically reflected and does not permeate. The top and bottom faces of each IAS binary mask, artificially made due to the length truncation, were extended with its reflective copies (mirroring boundary condition) to avoid geometrical discontinuity in diffusion simulations. In our simulations, each random walker diffused with a step duration $\delta t = 8.74 \times 10^{-5}$ ms and step length $\sqrt{6D_0\delta t} = 0.0324$ μm for the maximal diffusion time $t = 500$ ms, with 2×10^5 walkers per axon. For all our simulations, we set the intrinsic diffusivity $D_0 = 2$ $\mu\text{m}^2/\text{ms}$ in agreement with the recent *in vivo* experiments [84].

The time complexity of the simulator, i.e., the number of basic arithmetic operations performed, linearly increases with the diffusion time and the number of random walkers. We ran the simulations on an NVIDIA Tesla V100 GPU at the NYU Langone Health BigPurple high-performance computing cluster. In our settings, the average simulation time within a single intra-axonal space was 16 min, corresponding to about 90 axons per 24 hours, such that 36,363 axons considered in this work would take over 13 months to simulate.

Fick-Jacobs equation

In what follows, we assume diffusion in a *straight* tube aligned along x , with varying cross-section $A(x)$ along its length, and relate the diffusion coefficient $D(t)$ to the statistics of $A(x)$. The case of long-wave undulations on top of the cross-sectional variations will be considered later, in Sec. *Effect of undulations* and in Supplementary Section *The harmonic undulation model*.

Microscopically, the evolution of a three-dimensional particle density $\Psi(t; x, \mathbf{r}_\perp)$ is governed by the diffusion equation

$$\partial_t \Psi = D_0 \nabla^2 \Psi, \quad \nabla^2 = \partial_x^2 + \partial_{\mathbf{r}_\perp}^2, \quad (6)$$

with a 3d Laplace operator ∇^2 , and the boundary condition of zero particle flux through the tube walls. We are interested in integrating out the “fast” transverse degrees of freedom \mathbf{r}_\perp and deriving the “slow” effective 1d dynamics for times $t \gg A(x)/D_0$ over which the density across the transverse dimensions \mathbf{r}_\perp equilibrates. In this regime, $\Psi(t; x, \mathbf{r}_\perp) \simeq \Psi(t, x)$ becomes independent of \mathbf{r}_\perp , and the dynamics is described in terms of the 1d density

$$\psi(x) = \Psi(x)A(x). \quad (7)$$

This implies the adiabaticity of $A(x)$ varying slowly on the scale of typical axon radius $\sqrt{A/\pi}$. Under these assumptions, the 1d current density

$$J(x) = -D_0 A(x) \partial_x \left(\frac{\psi(x)}{A(x)} \right) \quad (8)$$

defines the FJ equation, Eq. (4) in the main text, for $\psi(x, t)$ via the 1d conservation law

$$\partial_t \psi(t, x) = -\partial_x J(x). \quad (9)$$

Tortuosity limit D_∞ at $t \rightarrow \infty$, Eq. (2)

Analogously to the problem of resistances in series, let us impose a finite 3d density jump $\Delta\Psi$ across the tube length L . Splitting the tube into small segments of lengths l_i , $\sum_i l_i = L$, full coarse-graining means that the transient processes die out, such that $\partial_t \Psi \equiv 0$, and current in each cross-section $J(x) = J_i = \text{const}$. According to Eq. (8), this current

$$-J = D_0 A_i \frac{\Delta\Psi_i}{l_i} \equiv D_\infty \bar{A} \frac{\Delta\Psi}{L} \quad (10)$$

defines the coarse-grained effective diffusion constant D_∞ , much like dc conductivity. Plugging the net jump

$$\Delta\Psi = \sum_i \Delta\Psi_i = \frac{J}{D_0} \sum_i \frac{l_i}{A_i} \equiv \frac{JL}{D_0} \left\langle \frac{1}{A(x)} \right\rangle$$

into Eq. (10), we obtain Eq. (2) from the main text.

Asymptotic approach of D_∞ , Eq. (3)

Let us separate the constant and the spatially varying terms in the FJ equation, Eq. (4):

$$\begin{aligned} \partial_t \psi(t, x) &= D_0 \partial_x^2 \psi(t, x) - D_0 \partial_x [y(x) \psi(t, x)], \\ y(x) &= \partial_x \ln \alpha(x). \end{aligned} \quad (11)$$

The last term defines the perturbation, Fig. 4a,

$$\mathcal{V} \psi \equiv -D_0 \partial_x [y(x) \psi(t, x)]. \quad (12)$$

The Green’s function (the fundamental solution) of Eq. (11) corresponds to the operator inverse

$$(\mathcal{L}_0 - \mathcal{V})^{-1} = G^{(0)} + G^{(0)} \mathcal{V} G^{(0)} + G^{(0)} \mathcal{V} G^{(0)} \mathcal{V} G^{(0)} + \dots$$

that has a form of the Born series (Fig. 4b). Physically, this series represents a total probability of propagating from x_1 to x_2 over time t as a sum of mutually exclusive events of propagating without scattering; scattering off the heterogeneities $\alpha(x)$ $n = 1$ time; $n = 2$ times; and so on. Here $\mathcal{L}_0 = \partial_t - D_0 \partial_x^2$ is the free diffusion operator, whose inverse defines the Green’s function of the free diffusion equation, diagonal in the Fourier domain:

$$G^{(0)} = \mathcal{L}_0^{-1} \rightarrow G_{\omega, q}^{(0)} = \frac{1}{-i\omega + D_0 q^2}. \quad (13)$$

Disorder-averaging of the Born series turns the products $\sim \mathcal{V} \dots \mathcal{V}$ into n -point correlation functions of $y(x)$,

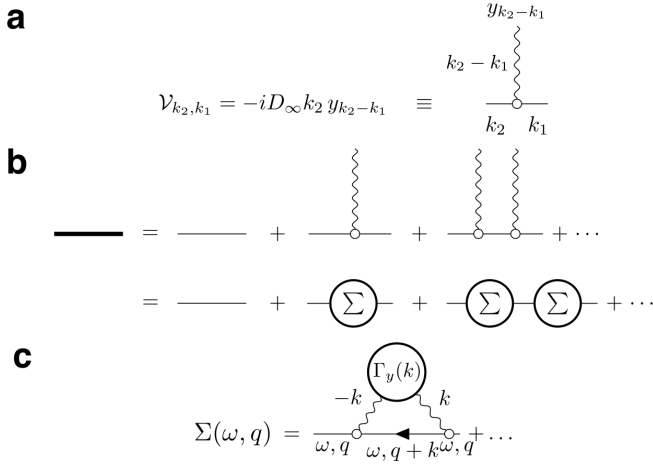


FIG. 4. **Feynman diagrams for the disorder averaging of the Green's function of Eq. (11).** (a) The dashed line represents an elementary scattering act off the static disorder potential (12) corresponding to the scattering vertex $\mathcal{V}(\cdot) = -D_\infty \partial_x (y(x) \cdot)$, Eq. (14), where for $t \rightarrow \infty$, we substitute $D_0 \rightarrow D_\infty$ (see text after Eq. (15)). In the Fourier representation, the scattering momentum (wave vector) is conserved at each scattering event: the sum of incoming momenta (k_1 and $k_2 - k_1$) equals the outgoing momentum k_2 . Since the disorder is static, the “energy” (frequency ω) is conserved in all diagrams. (b) The full Green's function (15), represented by the bold line, is given by the Born series, where propagation between scatterings is described by the free Green's functions $G^{(0)}$, Eq. (13) (thin lines). Averaging over the disorder turns the products $y(x_1) \dots y(x_n)$ into the corresponding n -point correlation functions; the sum of all 1-particle-irreducible diagrams (which cannot be split into two parts by cutting a single $G^{(0)}$ line) is by definition the self-energy part $\Sigma(\omega, q)$. (c) To the lowest (second) order, $\Sigma(\omega, q)$ is given by a single Feynman diagram (16) with the two-point correlation function $\Gamma_y(k)$, Eq. (17).

Fig. 4b, and makes the resulting propagator translation-invariant. This warrants working in the Fourier domain, such that the perturbation Eq. (12) corresponds to the vertex operator

$$\mathcal{V}_{k_2, k_1} = -iD_0 k_2 y_{k_2 - k_1} \quad (14)$$

as shown in Fig. 4a, where the wavy line represents an elementary scattering event with an incoming momentum $k_2 - k_1$ transferred to the particle with momentum k_1 , such that it proceeds with momentum k_2 .

According to the effective medium theory formalism (see, e.g., refs. [53, 55, 85, 86]), finding the disorder-averaged Green's function

$$G_{\omega, q} = \int dx dt e^{i\omega t - iqx} G_{t, x} = \frac{1}{-i\omega + D_0 q^2 - \Sigma(\omega, q)} \quad (15)$$

of Eq. (11) entails summing 1-particle-irreducible Feynman diagrams up to all orders in \mathcal{V} , that contribute to the self-energy part $\Sigma(\omega, q)$. This is, in general, impossible analytically.

However, following the intuition of ref. [53], the treatment simplifies in the limit of long t when coarse-graining over a large diffusion length $\ell(t)$ homogenizes the structural disorder $\alpha(x)$, by effectively suppressing its Fourier components $\alpha(q)$ or $y(q)$ with $q \gtrsim 1/\ell(t)$, as schematically depicted in Fig. 2d of the main text. At this point, the original free diffusivity D_0 gets renormalized down to D_∞ , Eq. (2), and what matters is the *residual* scattering off the long-wavelength heterogeneities; the latter are *suppressed* by the factor $\sim \sqrt{l_c/\ell(t)} \ll 1$ due to coarse-graining over the diffusion length $\ell(t) \gg l_c$ beyond the disorder correlation length l_c . Developing the perturbation theory around this Gaussian fixed point entails changing $D_0 \rightarrow D_\infty$ in the free propagator (13) and the scattering vertex (14). Hence, for sufficiently long times t , the perturbation (14) can be assumed to be small (essentially, being smoothed over the domains of size $\sim \ell(t)$), and the leading-order correction to the free propagator (13) with $D_0 \rightarrow D_\infty$ is determined by the lowest-order contribution to the self-energy part

$$\Sigma(\omega, q) = -D_\infty^2 \int \frac{dk}{2\pi} \frac{q(k+q) \Gamma_y(k)}{-i\omega + D_\infty(k+q)^2}, \quad (16)$$

where

$$\Gamma_y(q) = \frac{y(-q)y(q)}{L} \equiv q^2 \Gamma_\eta(q). \quad (17)$$

Here we introduced

$$\eta(x) = \ln \alpha(x) = \ln \frac{A(x)}{A} \quad (18)$$

such that

$$\Gamma_\eta(q) = \frac{\eta(-q)\eta(q)}{L} \quad (19)$$

is its power spectral density. Note that for small variations $\delta\alpha = \alpha - 1$, $\eta(x) = \ln(1 + \delta\alpha(x)) \approx \delta\alpha(x)$ such that $\Gamma_\eta(q) \approx \Gamma_\alpha(q)$ for $q \neq 0$. However, our approach is non-perturbative in $\delta\alpha$ and is valid even for strongly heterogeneous axons.

Finally, we note that the expansion of the term $\Sigma(\omega, q)|_{\omega=0}$ starts with q^2 and renormalizes the diffusion constant D_∞ (determined from the dispersion relation $-i\omega + D_\infty q^2 = 0$ defining the low-frequency pole of the propagator (15) up to q^2). Hence, in our effective medium treatment, we need to subtract this term from the self-energy part (16). Expanding

$$\Sigma(\omega, q) - \Sigma(\omega, q)|_{\omega=0} \equiv -\delta\mathcal{D}(\omega)q^2 + \mathcal{O}(q^4)$$

provides the dispersive contribution

$$\delta\mathcal{D}(\omega) = -i\omega D_\infty \int \frac{dk}{2\pi} \Gamma_\eta(k) \frac{-i\omega + 3D_\infty k^2}{(-i\omega + D_\infty k^2)^2} \quad (20)$$

to the overall low-frequency dispersive diffusivity $\mathcal{D}(\omega) = D_\infty + \delta\mathcal{D}(\omega)$ [55]. The corresponding long-time behavior of the *instantaneous* diffusion coefficient [37, 55]

$$D_{\text{inst}}(t) \equiv \frac{1}{2} \partial_t \langle x^2(t) \rangle = \int \frac{d\omega}{2\pi} \frac{\mathcal{D}(\omega)}{-i(\omega + i0)} e^{-i\omega t}$$

is found from Eq. (20) by deforming the contour of frequency integration downward from the equator of the Riemann sphere, to pick the 2nd-order residue at $\omega = -iD_\infty k^2$, yielding the long-time tail

$$\begin{aligned} \frac{\delta D_{\text{inst}}(t)}{D_\infty} &= \int \frac{dk}{2\pi} \Gamma_\eta(k) [1 + 2D_\infty k^2 t] e^{-D_\infty k^2 t} \\ &\equiv [1 - 2t \partial_t] \int \frac{dk}{2\pi} \Gamma_\eta(k) e^{-D_\infty k^2 t}. \end{aligned} \quad (21)$$

Note that Eqs. (20)–(21) are valid for any disorder of the tube shape, exemplified by the power spectral density (19). For our case of short-range disorder, defined by the finite plateau $\Gamma_\eta(k)|_{k \rightarrow 0} = \Gamma_0$, the above equations yield

$$\delta \mathcal{D}(\omega) \simeq \Gamma_0 \sqrt{-iD_\infty \omega} \quad \text{and} \quad \delta D_{\text{inst}}(t) \simeq \Gamma_0 \sqrt{\frac{D_\infty}{\pi t}}.$$

The dispersive $\delta \mathcal{D}(\omega)$ gives the result for $\mathcal{D}(\omega)$ quoted after Eq. (4) in the main text; its real part can be measured with oscillating gradients [37]. The corresponding *cumulative* diffusion coefficient

$$D(t) \equiv \frac{1}{2t} \langle x^2(t) \rangle = \frac{1}{t} \int_0^t dt' D_{\text{inst}}(t')$$

measured using pulse-gradient dMRI, acquires the $1/\sqrt{t}$ tail that is double the tail in $D_{\text{inst}}(t)$ above, yielding Eq. (1) with c_D given by Eq. (3). The above power law tails emerge when $\Gamma_\eta(q) \approx \Gamma_0$ does not appreciably vary on the (small) wavevector scale $0 \leq q \lesssim 1/\ell$, given by the reciprocal of the diffusion length $\ell \sim \sqrt{D_\infty/\omega} \sim \sqrt{D_\infty t}$, i.e., the disorder in $\eta(x)$ has been coarse-grained past its correlation length l_c . Equivalently, at such large scales $\ell \gg l_c$, the two-point correlation function

$$\Gamma_\eta(x) \equiv \langle \eta(x)\eta(0) \rangle = \int \frac{dq}{2\pi} e^{iqx} \Gamma_\eta(q)$$

of the variations of $\ln \alpha(x)$ can be considered local: $\Gamma_\eta(x) \simeq \Gamma_0 \delta(x)$.

Universality classes of tube shape fluctuations and Fick-Jacobs dynamics

While short-range disorder is most widespread, there exist distinct disorder universality classes [53, 87], characterized by the structural exponent p of their power spectral density at low wavevectors q , with short-range disorder corresponding to $p = 0$. For our purposes, consider the small-wavevector fluctuations of $\ln \alpha(x)$:

$$\Gamma_\eta(q) \simeq C|q|^p, \quad q \rightarrow 0. \quad (22)$$

We can call random tubes with $p > 0$ *hyperuniform* [87] and with $p < 0$ — *hyperfluctuating*. Qualitatively, hyperuniform systems are similar to ordered states with suppressed large-scale fluctuations, whereas hyperfluctuating systems exhibit diverging fluctuations at large scales.

Equations (20) and (21) relate the dynamical exponent

$$\vartheta = \frac{p+1}{2} \quad (23)$$

in the power law tails ω^ϑ and $t^{-\vartheta}$ of the above diffusive metrics to the structural exponent p in one spatial dimension, generalizing the purely-diffusion theory [53] onto the random FJ dynamics (4). Specifically, for the power spectral density (22),

$$\begin{aligned} \frac{\delta D_{\text{inst}}(t)}{D_\infty} &= \frac{(1+2\vartheta)\Gamma(\vartheta)}{2\pi} \frac{C}{(D_\infty t)^\vartheta}; \\ \frac{\delta \mathcal{D}(\omega)}{D_\infty} &= \frac{(1+2\vartheta)C}{2 \sin \pi \vartheta} \left(\frac{-i\omega}{D_\infty} \right)^\vartheta; \\ \frac{\delta D(t)}{D_\infty} &= \frac{(1+2\vartheta)\Gamma(\vartheta)}{2\pi(1-\vartheta)} \frac{C}{(D_\infty t)^\vartheta}, \quad \vartheta < 1, \end{aligned} \quad (24)$$

where $\Gamma(\vartheta)$ is the Euler's Γ -function. The last equation, for the $D(t)$ tail, is only valid for sufficiently slow tails, $\vartheta < 1$, corresponding to $p < 1$, i.e., to the tubes where fluctuations are not too suppressed; otherwise, the $1/t$ tail in $D(t)$ will conceive the true ϑ [53]. It is easy to check that for $p = 0$ and $C \rightarrow \Gamma_0$, Eqs. (24) correspond to the above results for the short-range disorder.

Effect of undulations

Let us now consider the effect of long-wavelength undulations (Supplementary Fig. S8) on top of local variations of $A(x)$. Since the undulation wavelength $\lambda \sim 30 \mu\text{m}$ [50] is an order of magnitude greater than the correlation length of $A(x)$, in Supplementary Section *The harmonic undulation model* we use this separation of scales to establish that an undulation results in a faster-decaying, $\sim 1/t$ tail in $D(t)$, which is beyond the accuracy of our main result (1) due to the short-range disorder in $A(x)$. Furthermore, the net undulation effect on Eqs. (1)–(3) up to $\mathcal{O}(1/\sqrt{t})$ is in the renormalization of the entire $D(t)$ by the factor $1/\xi^2$. Namely, for the i -th axon,

$$D_i(t) = \frac{D_{l,i}(t)}{\xi_i^2}, \quad (25)$$

Supplementary Eq. (S22), where the sinuosity $\xi_i = L_i/L_{x,i} \geq 1$ is the ratio of the arc to Euclidean length. Here, $D_{l,i}(t)$ is calculated in a “stretched” (“unrolled”) axon, i.e., using the arc length $l(x)$ instead of x , with $\alpha(x) \rightarrow \alpha(l)$, such that, technically, $\langle 1/\alpha \rangle \equiv \langle 1/\alpha(l) \rangle$, and similar for Γ_0 , in Fig. 2.

Practically, to parameterize the geometry of each axon by its arc length l , we evaluate an axonal cross-section $A(l)$ within a plane perpendicular to the axonal skeleton at each point $l(x)$ along its length. This effectively unrolls (stretches) the axon. The values of $A(l)$ along the skeleton are spline-interpolated and then sampled uniformly at $dl = 0.1 \mu\text{m}$ intervals. This equidistant sampling of

the curve skeleton ensures a uniformly spaced Fourier conjugate variable dq for calculating the power spectral density $\Gamma_\eta(q)$.

Axon's volume is determined via $\int dl A_i(l) \equiv \bar{A}_i L_i$, which also defines its average cross-sectional area \bar{A}_i , where $L_i = \int dl$ is the arc length. This volume measurement is used for volume-weighting the individual axonal contributions $D_i(t)$, Eq. (25), with weights $w_i \propto \bar{A}_i L_i$, to the ensemble diffusion coefficient $D(t)$ along the tract.

Statistics and reproducibility

Effect size: We define a nonparametric measure of effect size between two distributions X and Y as

$$d_{\text{eff}} = \frac{Q_{0.5}(X) - Q_{0.5}(Y)}{\text{PMAD}_{XY}}, \quad (26)$$

where $Q_{0.5}$ is the median of the distribution, and

$$\text{PMAD}_{XY} = \sqrt{\frac{(n_X - 1)\text{MAD}_X^2 + (n_Y - 1)\text{MAD}_Y^2}{n_X + n_Y - 2}}$$

is the pooled median absolute deviation, where MAD calculates the median absolute deviation using the Hodges-Lehmann estimator [88].

Class imbalance: To address the class imbalance when performing SVMs to separate between sham-operated and TBI axons, we randomly sub-sampled the dataset with the bigger number of axons to match the size of the class with fewer axons.

Supplementary Information

Scattering approach to diffusion quantifies axonal damage in brain injury

Ali Abdollahzadeh^{1,2,*}, Ricardo Coronado-Leija¹, Hong-Hsi Lee³, Alejandra Sierra², Els Fieremans¹, Dmitry S. Novikov¹

¹Center for Biomedical Imaging, Department of Radiology, New York University School of Medicine, New York, NY, USA

²A.I. Virtanen Institute for Molecular Sciences, University of Eastern Finland, Kuopio, Finland

³Athinoula A. Martinos Center for Biomedical Imaging, Department of Radiology, Massachusetts General Hospital, Harvard Medical School, Boston, MA, USA

*ali.abdollahzadeh@nyulangone.org

ESTIMATION OF THE $\Gamma_\eta(q)$ PLATEAU AT $q \rightarrow 0$

Determining Γ_0 from the power spectral density $\Gamma_\eta(q)$ of axons, especially for shorter axons with only a few low- q Fourier harmonics, requires a robust solution. For that we practically fit a polynomial of the form $\gamma q^2 + \Gamma_0$ to $\Gamma_\eta(q)$ in the range $[q_{\min}, q_{\max}]$, where $q_{\min} = 2\pi/L$ is the smallest accessible q , and q_{\max} is defined as the spatial frequency for which the small- q variance of the fluctuations is the fraction β of the total variance, i.e.,

$$\int_0^{q_{\max}} \frac{dq}{2\pi} \Gamma_\eta(q) = \beta \cdot \int_0^\infty \frac{dq}{2\pi} \Gamma_\eta(q). \quad (\text{S1})$$

We empirically fixed $\beta = 0.93$ for all EM axons and 0.98 for all synthetic axons in our analysis.

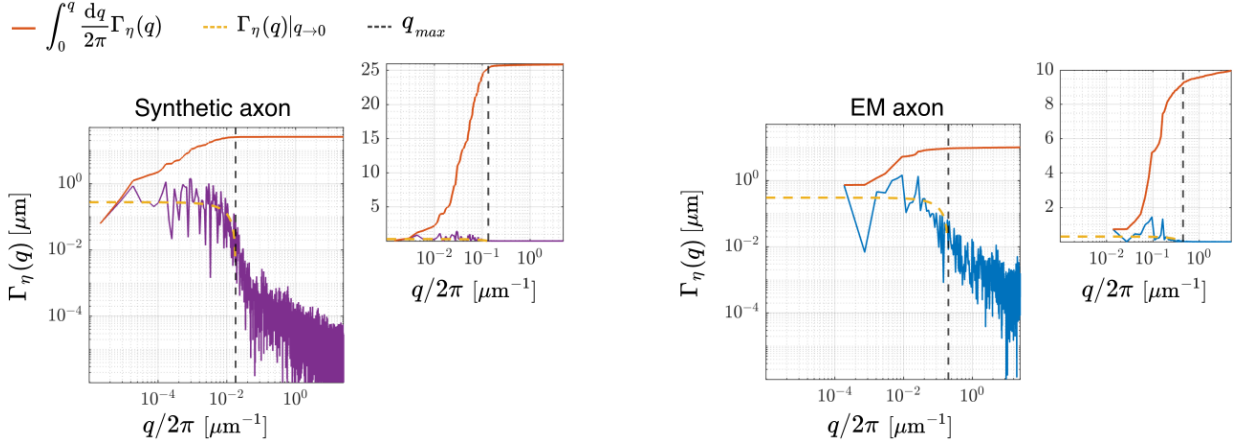


FIG. S1. **Estimation of Γ_0 .** Estimating Γ_0 from $\Gamma_\eta(q)$ for short axons with only a few low- q Fourier harmonics can be noisy. The $L = 500 \mu\text{m}$ synthetic axons (left panel) provide access to notably more relevant points at $q \rightarrow 0$ compared to the $L = 73.6 \mu\text{m}$ EM axons (right panel) for defining the plateau Γ_0 , with the polynomial fit shown by the yellow dashed line. The vertical dashed line indicates q_{\max} determined via Eq. (S1). Smaller insets show the same plots with the Γ_η -axis in the normal, rather than log scale.

Coarse-graining over the increasing diffusion length $\ell(t)$ suppresses $\Gamma_\eta(q)$, such that only the plateau Γ_0 “survives” for long t and governs the diffusive dynamics. Our approach to estimating Γ_0 as the constant term in the polynomial fit $\gamma q^2 + \Gamma_0$, is consistent with this physical picture. In Fig. 2d of the main text, the estimated $\Gamma_0 = 0.21 \pm 0.03$ (mean \pm std) remained unchanged for a range of diffusion times t_0, \dots, t_3 . The magnitude of the quadratic term γ increased substantially during coarse-graining: $\gamma = -5.23, -123.61, -265.04, -1331$ for t_0, \dots, t_3 , indicating a progressively stronger suppression of the finite- q Fourier harmonics.

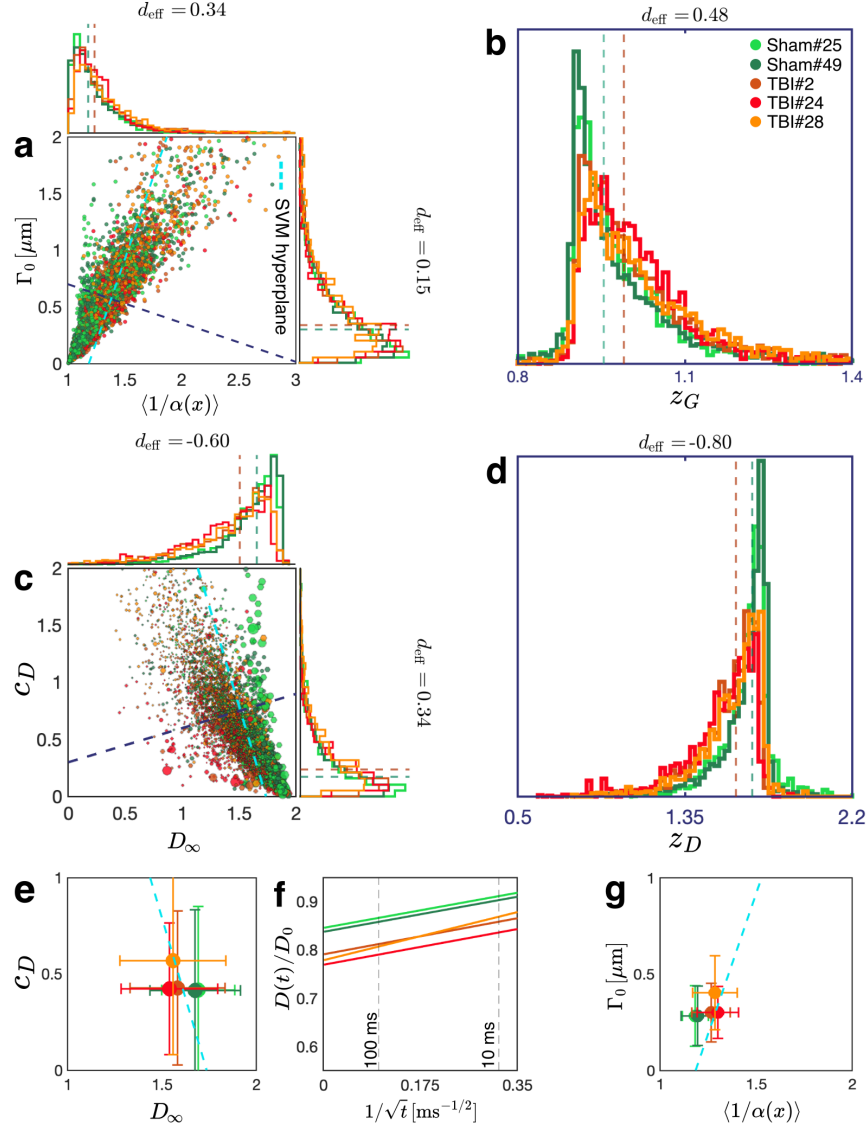
EFFECT OF CHRONIC TBI ON AXON MORPHOLOGY AND $D(t)$ 

FIG. S2. **Effect of chronic TBI on axon morphology and $D(t)$ from the contralateral cingulum.** (a) Geometric tortuosity $\langle 1/\alpha \rangle$, Eq. (2), and the variance Γ_0 of long-range cross-sectional fluctuations entering Eq. (3), are plotted for myelinated axons segmented from the contralateral cingulum of sham-operated (shades of green; $N = 4,580$) and TBI (shades of red; $N = 4,580$) rats. (b) The optimal linear combination z_G of the morphological parameters is derived from a trained support vector machine (SVM). Projecting the points onto the dark blue dashed line in (a) perpendicular to the SVM hyperplane constitutes the maximal separation between the two groups. (c) Predicted individual axon diffusion parameters $D_{\infty,i}$ and $c_{D,i}$ from Eqs. (2)–(3) plotted for myelinated axons in (a). The size of each point reflects its weight w_i in the net dMRI-accessible $D(t)$, proportional to the axon volume. (d) The optimal SVM-based linear combination z_D of the diffusion parameters is derived by projecting the points onto the dark blue dashed line in (c) perpendicular to the corresponding SVM hyperplane. The dashed lines overlaid on the distributions in (a–d) represent the medians of the pool of two sham-operated datasets and of the pool of three TBI datasets. (e) The macroscopic diffusivity parameters c_D and D_∞ for each animal are obtained by volume-weighting the individual axonal contributions $D_{\infty,i}$ and $c_{D,i}$. The SVM hyperplane (cyan dashed line) is the same as that for the diffusion parameters of individual axons in (c). (f) Predicting the along-tract $D(t)/D_0$ as a function of $1/\sqrt{t}$, Eq. (1), based on the overall D_∞ and c_D in (e). (g) The effect of TBI on the ensemble-averaged geometry is illustrated by transforming the macroscopic ensemble diffusivity in (e,f), as if from an MRI measurement, back onto the space of morphological parameters $\langle 1/\alpha \rangle$ and Γ_0 , via inverting Eqs. (2)–(3). The SVM hyperplane (cyan dashed line) is the same as that for the morphological parameters of individual axons in (a). Error bars correspond to standard deviations of $\langle 1/\alpha \rangle$ and Γ_0 , based on errors in measuring the volume-weighted D_∞ and c_D in (e).

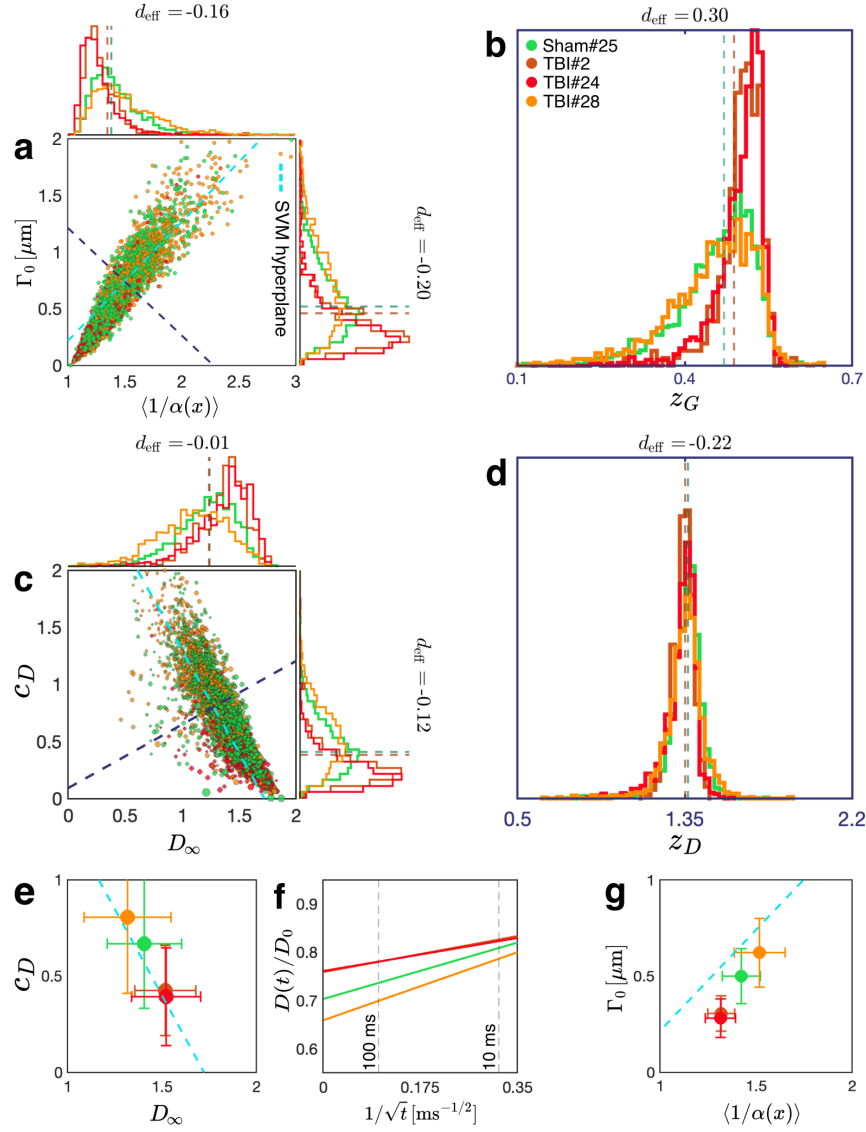


FIG. S3. Effect of chronic TBI on axon morphology and $D(t)$ from the ipsilateral corpus callosum. (a) Geometric tortuosity $\langle 1/\alpha \rangle$, Eq. (2), and the variance Γ_0 of long-range cross-sectional fluctuations entering Eq. (3), are plotted for myelinated axons segmented from the ipsilateral corpus callosum of sham-operated (shades of green; $N = 2,703$) and TBI (shades of red; $N = 2,703$) rats. (b) The optimal linear combination z_G of the morphological parameters is derived from a trained support vector machine (SVM). Projecting the points onto the dark blue dashed line in (a) perpendicular to the SVM hyperplane constitutes the maximal separation between the two groups. (c) Predicted individual axon diffusion parameters $D_{\infty,i}$ and $c_{D,i}$ from Eqs. (2)–(3) plotted for myelinated axons in (a). The size of each point reflects its weight w_i in the net dMRI-accessible $D(t)$, proportional to the axon volume. (d) The optimal SVM-based linear combination z_D of the diffusion parameters is derived by projecting the points onto the dark blue dashed line in (c) perpendicular to the corresponding SVM hyperplane. The dashed lines overlaid on the distributions in (a–d) represent the medians of the pool of two sham-operated datasets and of the pool of three TBI datasets. (e) The macroscopic diffusivity parameters c_D and D_∞ for each animal are obtained by volume-weighting the individual axonal contributions $D_{\infty,i}$ and $c_{D,i}$. The SVM hyperplane (cyan dashed line) is the same as that for the diffusion parameters of individual axons in (c). (f) Predicting the along-tract $D(t)/D_0$ as a function of $1/\sqrt{t}$, Eq. (1), based on the overall D_∞ and c_D in (e). (g) The effect of TBI on the ensemble-averaged geometry is illustrated by transforming the macroscopic ensemble diffusivity in (e,f), as if from an MRI measurement, back onto the space of morphological parameters $\langle 1/\alpha \rangle$ and Γ_0 , via inverting Eqs. (2)–(3). The SVM hyperplane (cyan dashed line) is the same as that for the morphological parameters of individual axons in (a). Error bars correspond to standard deviations of $\langle 1/\alpha \rangle$ and Γ_0 , based on errors in measuring the volume-weighted D_∞ and c_D in (e).

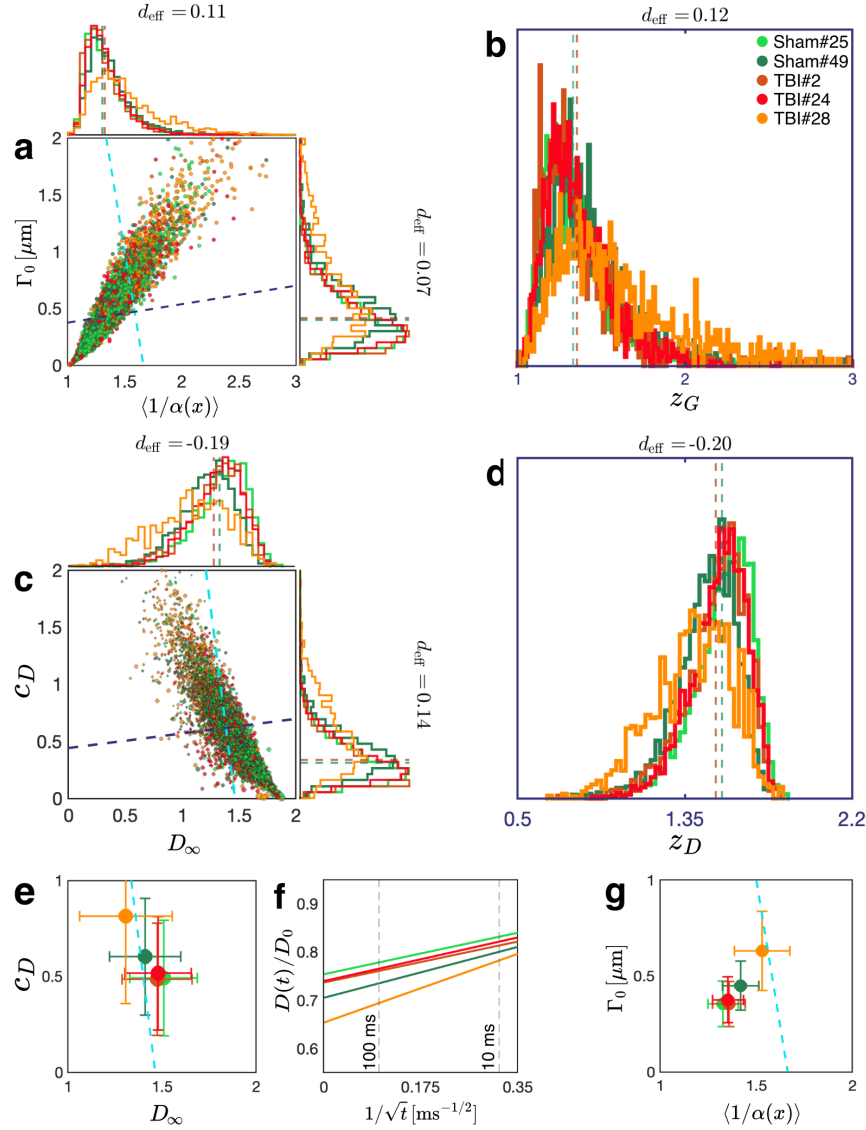


FIG. S4. **Effect of chronic TBI on axon morphology and $D(t)$ from the contralateral corpus callosum.** (a) Geometric tortuosity $\langle 1/\alpha \rangle$, Eq. (2), and the variance Γ_0 of long-range cross-sectional fluctuations entering Eq. (3), are plotted for myelinated axons segmented from the contralateral corpus callosum of sham-operated (shades of green; $N = 4,080$) and TBI (shades of red; $N = 4,080$) rats. (b) The optimal linear combination z_G of the morphological parameters is derived from a trained support vector machine (SVM). Projecting the points onto the dark blue dashed line in (a) perpendicular to the SVM hyperplane constitutes the maximal separation between the two groups. (c) Predicted individual axon diffusion parameters $D_{\infty,i}$ and $c_{D,i}$ from Eqs. (2)–(3) plotted for myelinated axons in (a). The size of each point reflects its weight w_i in the net dMRI-accessible $D(t)$, proportional to the axon volume. (d) The optimal SVM-based linear combination z_D of the diffusion parameters is derived by projecting the points onto the dark blue dashed line in (c) perpendicular to the corresponding SVM hyperplane. The dashed lines overlaid on the distributions in (a–d) represent the medians of the pool of two sham-operated datasets and of the pool of three TBI datasets. (e) The macroscopic diffusivity parameters c_D and D_∞ for each animal are obtained by volume-weighting the individual axonal contributions $D_{\infty,i}$ and $c_{D,i}$. The SVM hyperplane (cyan dashed line) is the same as that for the diffusion parameters of individual axons in (c). (f) Predicting the along-tract $D(t)/D_0$ as a function of $1/\sqrt{t}$, Eq. (1), based on the overall D_∞ and c_D in (e). (g) The effect of TBI on the ensemble-averaged geometry is illustrated by transforming the macroscopic ensemble diffusivity in (e,f), as if from an MRI measurement, back onto the space of morphological parameters $\langle 1/\alpha \rangle$ and Γ_0 , via inverting Eqs. (2)–(3). The SVM hyperplane (cyan dashed line) is the same as that for the morphological parameters of individual axons in (a). Error bars correspond to standard deviations of $\langle 1/\alpha \rangle$ and Γ_0 , based on errors in measuring the volume-weighted D_∞ and c_D in (e).

MOMENTS OF AXON RADIUS DISTRIBUTION CONTRIBUTING TO THE TORTUOSITY VERSUS EFFECTIVE AXON RADIUS

For a heterogeneous axon population, both the tortuosity $\langle 1/\alpha \rangle$ and the effective MR radius [89] r_{eff} in previously developed axon radius mapping with dMRI [90] (by applying extremely strong gradients) involve the moments of axon radius distribution. Here, we compare the contributions of such moments to both quantities and show that tortuosity provides a similar degree of separation between TBI and sham rats, yet it involves lower-order moments of radius.

Effective axon MR radius for an ensemble of irregularly-shaped axons

Diffusion MRI-measured effective axon radius (in the wide-pulse regime) corresponds to the ratio of the 6th and 2nd moments of the distribution of straight cylinders [89]:

$$r_{\text{eff}} = \left(\frac{\langle r^6 \rangle_{\text{ensemble}}}{\langle r^2 \rangle_{\text{ensemble}}} \right)^{1/4}. \quad (\text{S2})$$

This comes from the Neuman's result [91] for the signal attenuation, $-\ln S \propto r^4$, that is subsequently volume-weighted, such that effectively, r_{eff}^4 is measured to the lowest order in the diffusion attenuation over the ensemble of cylinders.

Recently, it was shown [57] that the same expression (S2) applies for an effective MR radius measured in a *single axon* with variable cross-section, i.e., the cross-sections of an irregularly-shaped axon in 3 dimensions effectively act as an ensemble of independent 2-dimensional disks (or uniform cylinders). In other words, for a single axon, the effective MR radius is given by Eq. (S2) where the ensemble averaging $\langle \dots \rangle_{\text{ensemble}} \rightarrow \langle \dots \rangle = \frac{1}{L} \int dx \dots$ is substituted by the average along the axon axis x , as in the main text.

In our case of an ensemble of irregularly shaped axons, the averaging both along each axon axis and over the ensemble of axons yields

$$r_{\text{eff}}^4 = \sum_i w_i r_{\text{eff},i}^4 = \frac{\sum_i \langle r_i^2(x) \rangle \langle r_i^6(x) \rangle / \langle r_i^2(x) \rangle}{\sum_j \langle r_j^2(x) \rangle} = \frac{\sum_i \langle r_i^6(x) \rangle}{\sum_j \langle r_j^2(x) \rangle} \quad (\text{S3})$$

where, as discussed in the main text, the weights are proportional to the mean cross-sectional area $\bar{A}_i = \langle A_i(x) \rangle$,

$$w_i = \frac{\bar{A}_i}{\sum_j \bar{A}_j} = \frac{\langle r_i^2(x) \rangle}{\sum_j \langle r_j^2(x) \rangle}, \quad \text{where} \quad A_i(x) = \pi r_i^2(x) \quad (\text{S4})$$

defines the equivalent radius $r_i(x)$ (as always, we assume that axons have the same length). As everywhere in this paper, the angular brackets denote averaging along the axon axis x . In other words, the effective radius (S3) corresponds to the ratio of the 6th and 2nd moments of the *joint distribution of equivalent axon radii* over cross-sections and axons — equivalent to slicing all axons into individual cross-sections and pooling all of them into one distribution.

Effective tortuosity for an ensemble of irregularly-shaped axons

Consider now the ensemble-averaged D_{∞} , assuming the same D_0 for all axons:

$$\frac{D_{\infty, \text{eff}}}{D_0} = \sum_i w_i \frac{D_{\infty, i}}{D_0} = \sum_i \frac{w_i}{\langle 1/\alpha_i(x) \rangle} = \sum_i \frac{w_i}{\langle 1/(1 + \delta\alpha_i(x)) \rangle}, \quad (\text{S5})$$

where expanding $\langle 1/(1 + \delta\alpha(x)) \rangle$ up to $(\delta\alpha(x))^2$, we can write Eq. (S5) as

$$\frac{D_{\infty, \text{eff}}}{D_0} = \sum_i \frac{w_i}{1 + \langle (\delta\alpha_i(x))^2 \rangle + \mathcal{O}((\delta\alpha_i(x))^3)} \simeq \sum_i w_i (1 - \langle (\delta\alpha_i(x))^2 \rangle). \quad (\text{S6})$$

Using the weights (S4) and $\langle (\delta\alpha_i(x))^2 \rangle = \langle A_i^2(x) \rangle / \bar{A}_i^2 - 1$, we can rewrite Eq. (S6) via the equivalent radii $r_i(x)$ as

$$\frac{D_{\infty, \text{eff}}}{D_0} \simeq 1 - \left[\frac{1}{\sum_j \langle r_j^2(x) \rangle} \sum_i \frac{\langle r_i^4(x) \rangle}{\langle r_i^2(x) \rangle} - 1 \right] \Rightarrow \frac{D_0}{D_{\infty, \text{eff}}} \simeq \frac{1}{\sum_j \langle r_j^2(x) \rangle} \sum_i \frac{\langle r_i^4(x) \rangle}{\langle r_i^2(x) \rangle}. \quad (\text{S7})$$

Thus, the tortuosity is dominated by the 2nd and 4th moments of equivalent radii (i.e., less affected by the tail of radius distribution). Yet, it cannot be expressed via moments of the *joint distribution* over cross-sections and axons.

Separating sham-operated and TBI with ensemble-averaged r_{eff} and tortuosity

In Fig. S5, we compare the sensitivity of the effective tortuosity Eq. (S5) with that of the effective radius r_{eff} Eq. (S3). Both measures have approximately similar sensitivity in separating sham-operated and TBI datasets for all comparisons.

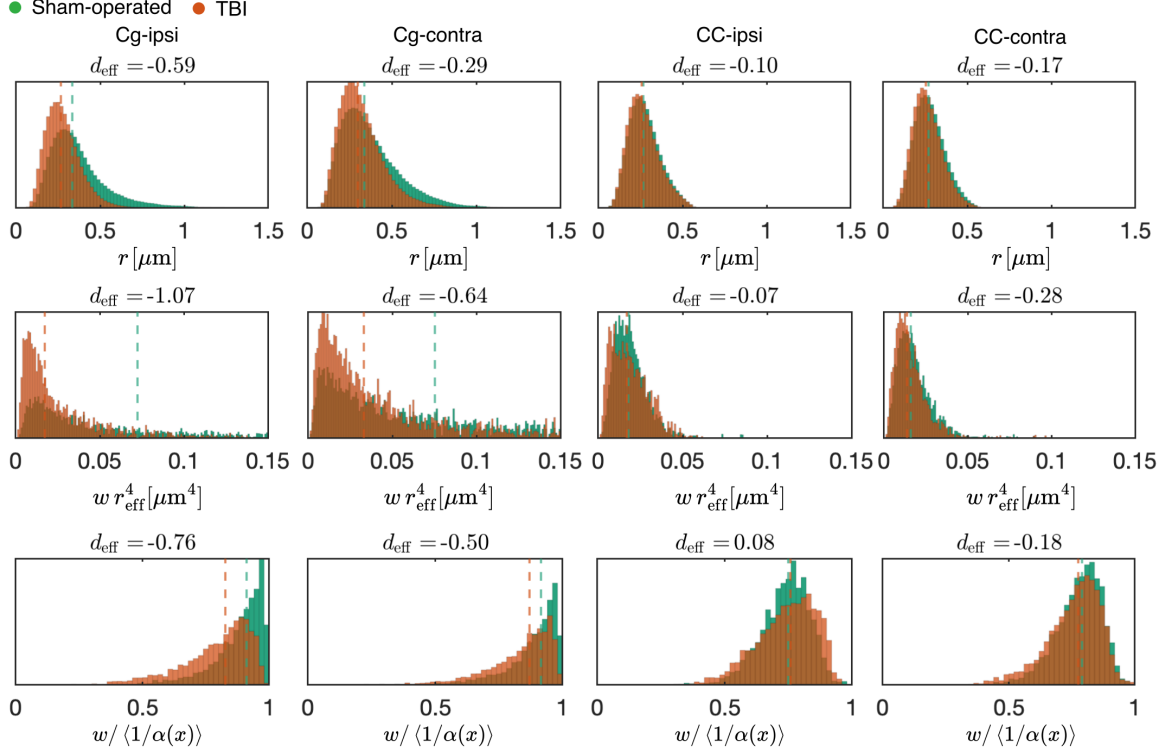


FIG. S5. **Sensitivity of tortuosity versus effective radius.** The top row shows histograms of axon radius across all axons and cross-sections in each considered brain region: Cg-ipsi ($N = 3,999$), Cg-contra ($N = 4,580$), CC-ipsi ($N = 2,703$), and CC-contra ($N = 4,080$). The histograms demonstrate the decrease in the axon radius caused by TBI on the ipsilateral side. The middle row shows histograms of volume-weighted effective MR radius $w r_{\text{eff}}^4$ across all axons in each region, entering the weighted average in Eq. (S3). The bottom row shows histograms of volume-weighted reciprocal tortuosity $w / \langle 1/\alpha(x) \rangle$ across all axons in each region, entering the weighted average in Eq. (S5). The reciprocal tortuosity (effectively averaged in a bulk measurement of D_∞) and the 4th power of effective MR radius r_{eff} (effectively averaged in a bulk measurement of axon radius) show similar effect sizes for separating sham-operated and TBI datasets. However, estimating r_{eff} requires very strong diffusion gradients. Dashed lines are the medians of the underlying distributions, exemplifying the macroscopically measured quantities.

THE SINGLE-BEAD MODEL

To get an intuition for the key quantity Γ_0 determining the amplitude Eq. (3) of the $1/\sqrt{t}$ tail Eq. (1) in $D(t)$, here we consider the *single-bead model* of a randomly-shaped axon. Namely, as mentioned in the main text, we represent an axon of length L with a normalized cross-sectional area $\alpha(x) = A(x)/\bar{A} \equiv e^{\eta(x)}$ as a set of N identical multiplicative beads with the shape $\eta_1(x)$ placed at random positions x_m on top of the uniform “background” η_0 without beads:

$$\eta(x) = \ln \alpha(x) = \eta_0 + \sum_{m=1}^N \eta_1(x - x_m), \quad (\text{S8})$$

such that the macroscopic bead density $\bar{n} = N/L$. For the power spectral density (19), we need the Fourier transform

$$\eta(q) = \eta_0 \cdot 2\pi\delta(q) + \eta_1(q) \sum_{m=1}^N e^{-iqx_m}. \quad (\text{S9})$$

Writing the square of the Dirac delta-function $\delta^2(q) = \delta(q)\delta(q=0) = (L/2\pi)\delta(q)$ (assuming $L \rightarrow \infty$), we obtain

$$\Gamma_\eta(q) = \frac{|\eta(q)|^2}{L} = 2\pi\eta_0 \left[\eta_0 + 2\frac{\zeta}{\bar{a}} \right] \delta(q) + |\eta_1(q)|^2 \Gamma_{\text{pos}}, \quad \Gamma_{\text{pos}}(q) = \frac{1}{L} \sum_{m,m'=1}^N e^{-iq(x_m - x_{m'})}, \quad (\text{S10})$$

where the “bead length”

$$\zeta = \eta_1(q)|_{q=0} = \int dx \eta_1(x),$$

and $\bar{a} = L/N = 1/\bar{n}$ is the mean interval between successive bead positions (i.e., the inverse number density \bar{n}).

Equation (S10) is so far very general. The statistics of bead placement are reflected in the particular functional form of the power spectral density $\Gamma_{\text{pos}}(q)$ of bead positions. In our model, we further assume that the successive intervals $a_m = x_{m+1} - x_m$ are independent and identically distributed random variables chosen from a probability density function (PDF) $P(a)$ with a finite mean \bar{a} and variance σ_a . This allows us to represent $\Gamma_{\text{pos}}(q)$ in terms of the parameters of $P(a)$. Assuming self-averaging in a large enough system ($N \gg 1$), we can substitute $\Gamma_{\text{pos}}(q)$ for a particular disorder realization by its expected value

$$\Gamma_{\text{pos}}(q) = \frac{1}{L} \sum_{m,m'=1}^N \left\langle e^{-iq(x_m - x_{m'})} \right\rangle = \frac{1}{L} \sum_{m=1}^N \left\langle 1 + \sum_{s=1} e^{-iq(a_1 + \dots + a_s)} + \sum_{s=1} e^{iq(a_1 + \dots + a_s)} \right\rangle = \bar{n} \left[1 + \frac{\tilde{p}_q}{1 - \tilde{p}_q} + \frac{\tilde{p}_q^*}{1 - \tilde{p}_q^*} \right], \quad (\text{S11})$$

where $\tilde{p}_q = \int da e^{-iqa} P(a)$ is the characteristic function of $P(a)$, and $*$ stands for the complex conjugation. The above disorder averaging was performed by representing $x_m - x_{m'} = \sum_{j=m'}^{m-1} a_j$, splitting the double sum into three terms (with $m = m'$, $m > m'$, and $m < m'$, where $s = m - m'$), and summing the geometric series in the limit $N = \bar{n}L \rightarrow \infty$. Representing the characteristic function \tilde{p}_q via its cumulants, $\tilde{p}_q = e^{-iq\bar{a} - q^2\sigma_a^2/2 + \dots}$ in Eq. (S11) and taking the limit $q \rightarrow 0$ by expanding \tilde{p}_q up to q^2 yields

$$\Gamma_{\text{pos}}(q)|_{q \rightarrow 0} = \frac{\sigma_a^2}{\bar{a}^3}. \quad (\text{S12})$$

Plugging Eq. (S12) into Eq. (S10) and taking the $q \rightarrow 0$ limit, we finally obtain

$$\Gamma_0 = \Gamma_\eta(q)|_{q \rightarrow 0} = \frac{\sigma_a^2}{\bar{a}} \phi^2, \quad \phi = \frac{\zeta}{\bar{a}}, \quad (\text{S13})$$

where the factor σ_a^2/\bar{a} characterizes the statistics of bead positions, and ϕ is a dimensionless length ratio that tells how pronounced the relative area modulation is. In Fig. S6, we decompose Γ_0 into its comprising factors, according to Eq. (S13), and quantify their separate TBI effect sizes in different brain regions.

In Fig. S7, we analyze the bead position statistics and its change in TBI in greater detail. The top row of Fig. S7 shows that the mean distance between successive beads \bar{a} decreases (and the bead density \bar{n} increases) in TBI axons compared to sham-operated animals. Notably, bead positions in TBI axons exhibit a smaller coefficient of variation σ_a/\bar{a} , suggesting a more ordered arrangement of the beads (middle row). To explore this further, we considered the power spectral density $\Gamma_{\text{pos}}(q)$ of bead positions, Eq. (S10). The finite plateau $\bar{a} \cdot \Gamma_{\text{pos}}|_{q \rightarrow 0} = (\sigma_a/\bar{a})^2$ in TBI is lower than that for the sham-operated dataset in the cingulum (bottom row), consistent with a lower coefficient of variation and a more ordered arrangement. (This can also be contrasted with a periodic arrangement: $\Gamma_{\text{pos}} \equiv 0$ for $q < 2\pi/\bar{a}$.)

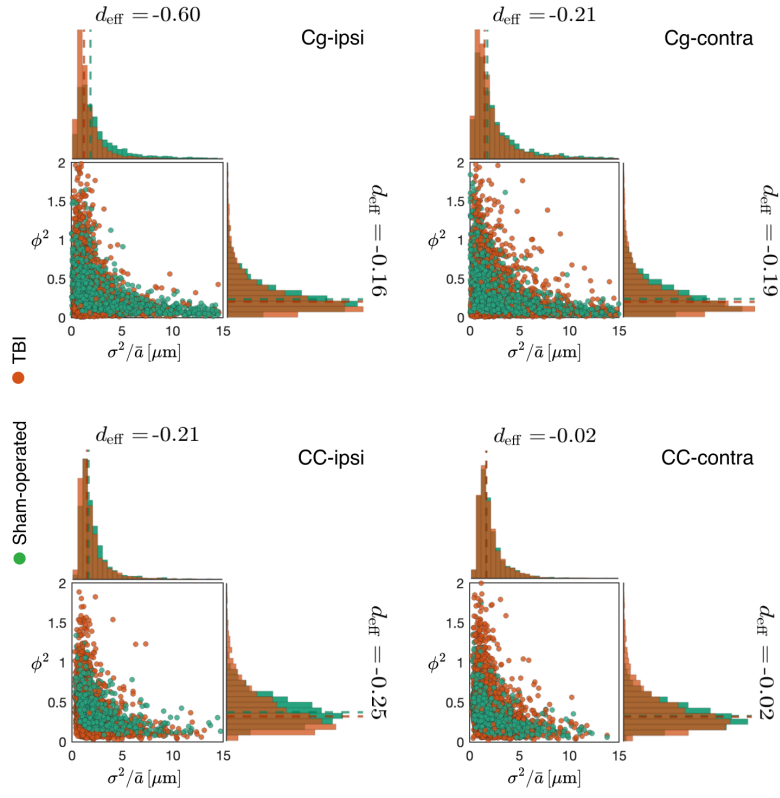


FIG. S6. **Geometric interpretation of Γ_0 .** Comparisons over Cg-ipsi ($N = 3,999$), Cg-contra ($N = 4,580$), CC-ipsi ($N = 2,703$), and CC-contra ($N = 4,080$) show that TBI caused a decrease σ_a^2/\bar{a} and decrease in the ϕ^2 .

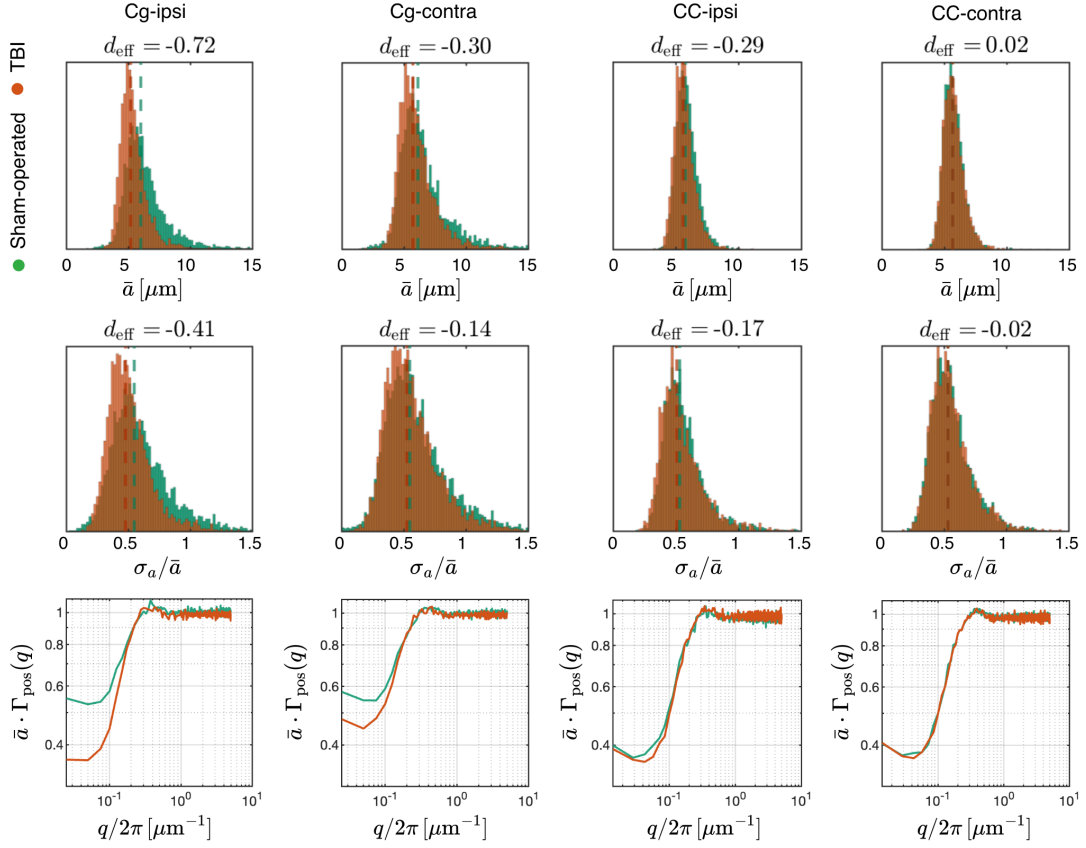


FIG. S7. **Statistics of bead positions.** Top row shows the distribution of the mean distance \bar{a} between successive beads for all myelinated axons from sham-operated and TBI animals in Cg-ipsi ($N = 3,999$), Cg-contra ($N = 4,580$), CC-ipsi ($N = 2,703$), and CC-contra ($N = 4,080$) datasets; TBI caused a substantial decrease in \bar{a} . The middle row shows the coefficient of variation σ_a/\bar{a} of bead positions. Interestingly, bead positions in TBI have a smaller variation than sham-operated datasets, indicating a more ordered placement. This can also be seen from the plateau $\bar{a} \cdot \Gamma_{\text{pos}}|_{q \rightarrow 0} = (\sigma_a/\bar{a})^2$, according to Eq. (S12) (bottom row). The lower plateau in TBI indicates a more ordered bead placement.

THE HARMONIC UNDULATION MODEL

Here, we extend the treatment of Gaussian diffusion along the axonal arc-length (Appendix E of Ref. [57]) onto the case of arbitrary, time-dependent $D(t)$. To quantify the effect of axonal undulations on diffusion metrics, we introduce sinuosity ξ defined as the ratio of the arc-length $L = \int dl$ of the axonal skeleton to its Euclidean length $L_x = \int dx$:

$$\xi = \frac{L}{L_x} = \frac{1}{L_x} \int \sqrt{(dx)^2 + |d\mathbf{w}|^2}, \quad (\text{S14})$$

where l is the coordinate along the skeleton, x is the coordinate along the main axis, and $\mathbf{w}(l)$ is the vector of the shortest distance between the skeleton and the main axis at each point l along the skeleton, Fig. S8a.

To understand the effect of undulation on diffusion along axons, we consider a sinusoidal undulation in one plane (the 1-harmonic model [57]):

$$w = w_0 \cos k_u x \quad (\text{S15})$$

where w_0 is the undulation amplitude, $k_u = 2\pi/\lambda$, and λ is the undulation wavelength. Expanding Eq. (S14) for the 1-harmonic model, we have

$$\begin{aligned} l(x) &\simeq \int_0^x dx \left(1 + \frac{(dw/dx)^2}{2} - \frac{(dw/dx)^4}{8} \right) \\ &= \int_0^x dx \left(1 + 2\epsilon \sin^2 k_u x + 2\epsilon^2 \sin^4 k_u x \right) = \xi x - (\epsilon - \epsilon^2) \frac{\sin 2k_u x}{2k_u} - \epsilon^2 \frac{\sin 4k_u x}{16k_u}, \end{aligned} \quad (\text{S16})$$

where $\epsilon \equiv (k_u w_0/2)^2 = (\pi w_0/\lambda)^2 \ll 1$, and sinuosity $\xi \simeq 1 + \epsilon - \frac{3}{4}\epsilon^2$. We now invert $l(x)$ perturbatively up to $\mathcal{O}(\epsilon^2)$:

$$x(l) \simeq \frac{l}{\xi} \left[1 + \frac{\epsilon}{2k_u l} \sin \frac{2k_u l}{\xi} - \frac{\epsilon^2}{2k_u l} \left(\sin 2k_u l - \frac{5}{8} \sin 4k_u l \right) \right]. \quad (\text{S17})$$

To get the above equation, we approximated $\sin 2k_u x \approx \sin(2k_u l/\xi) + (\epsilon/2) \sin 4k_u l$ up to $\mathcal{O}(\epsilon)$, and substituted $\sin 4k_u x$ with $\sin 4k_u l$ as that term is already $\mathcal{O}(\epsilon^2)$.

The cumulative axial diffusivity $D(t) \equiv \langle \delta x^2(t) \rangle / 2t$ along the main axis is given in terms of

$$\langle \delta x^2(t) \rangle = \frac{1}{L} \int [x(l) - x(l')]^2 G(t, l - l') dl dl', \quad (\text{S18})$$

where $G(t, l)$ is the disorder-averaged propagator of the Fick-Jacobs Eq. (4) taken along the arc length l (i.e. when the axonal undulations are straightened, as described in *Methods*). In other words, it is the EMT propagator (15) (in the time-space representation) of the FJ equation (11), where, instead of x , we work with the “unrolled” arc length coordinate l , and take into account scatterings off the fluctuations of $\alpha(l)$. As we stated in *Methods*, all the above analysis has been performed after such an unrolling — e.g., $\Gamma_\eta(q)$ is obtained in the arc length coordinates, with q in Fig. 2 being the Fourier variable conjugate to the cross-sectional area fluctuations along the arc length.

We now substitute $x(l)$ from Eq. (S17) into Eq. (S18). For that, we change variables to $l_+ = (l+l')/2$ and $l_- = l-l'$, and expand $[x(l) - x(l')]^2$ up to ϵ^2 , setting $\xi \rightarrow 1$ whenever the term is already $\mathcal{O}(\epsilon^2)$:

$$\begin{aligned} x(l) - x(l') &\simeq \frac{l_-}{\xi} + \frac{\epsilon}{k_u \xi} \cos \frac{2k_u l_+}{\xi} \sin \frac{k_u l_-}{\xi} - \frac{\epsilon^2}{k_u} \left[\cos 2k_u l_+ \sin k_u l_- - \frac{5}{8} \cos 4k_u l_+ \sin 2k_u l_- \right] + \mathcal{O}(\epsilon^3) \Rightarrow \\ [x(l) - x(l')]^2 &\simeq \left(\frac{l_-}{\xi} \right)^2 + \frac{\epsilon^2}{k_u^2} \cos^2 2k_u l_+ \sin^2 k_u l_- + \frac{2\epsilon l_-}{k_u \xi^2} \cos \frac{2k_u l_+}{\xi} \sin \frac{k_u l_-}{\xi} \\ &\quad - \frac{2\epsilon^2 l_-}{k_u} \left[\cos 2k_u l_+ \sin k_u l_- - \frac{5}{8} \cos 4k_u l_+ \sin 2k_u l_- \right] + \mathcal{O}(\epsilon^3). \end{aligned} \quad (\text{S19})$$

Integrating Eq. (S19) with the propagator $G(t, l_-)$ in Eq. (S18) implies the averaging with respect to l_+ over large L . This cancels all the oscillating terms, such that only the first two terms survive; in the second term, $\cos^2 2k_u l_+ \rightarrow \frac{1}{2}$ after averaging, and $\sin^2 k_u l_- = \frac{1}{2}[1 - \text{Re } e^{-2ik_u l_-}]$ yields the Fourier transform of $G(t, l_-)$. As a result,

$$\langle \delta x^2(t) \rangle \simeq \frac{1}{\xi^2} \int l_-^2 G(t, l_-) dl_- + \frac{\epsilon^2}{4k_u^2} [1 - G(t, q)|_{q=2k_u}] + \mathcal{O}(\epsilon^3). \quad (\text{S20})$$

From Eq. (S20), we conclude

$$D(t) = \frac{\langle \delta x^2(t) \rangle}{2t} \simeq \frac{1}{\xi^2} D_l(t) + \frac{\epsilon^2}{8k_u^2 t} [1 - G(t, q)|_{q=2k_u}]. \quad (\text{S21})$$

The second term in Eq. (S21) decays at least as fast as $1/t$ for any propagator G , while the $1/\sqrt{t}$ behavior all comes from the diffusion coefficient $D(t)$ renormalized by the $1/\xi^2$ factor:

$$D(t) \simeq \frac{1}{\xi^2} \left[D_{\infty, l} + \frac{c_{D, l}}{\sqrt{t}} \right]. \quad (\text{S22})$$

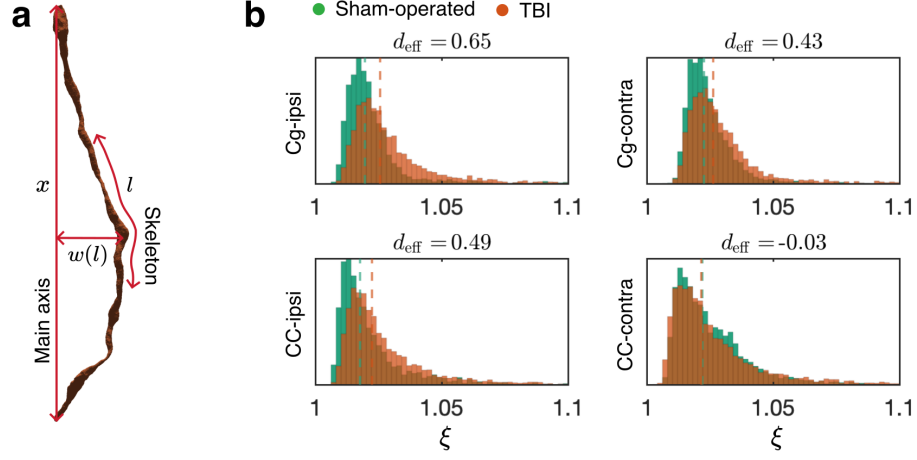


FIG. S8. **Axonal sinuosity.** TBI caused an increase in the axonal sinuosity ξ in the Cg-ipsi ($N = 3,999$), Cg-contra ($N = 4,580$), and CC-ipsi ($N = 2,703$), and had no effect on CC-contra ($N = 4,080$).

DESCRIPTION OF DATASETS

TABLE S1. **Description of the SBEM datasets.** We collected the SBEM images from the ipsi- and contralateral corpus callosum and cingulum of two sham-operated rats and three rats with traumatic brain injury (TBI). The images from the ipsilateral hemisphere of the sham #49 rat included only the cingulum. The order of the axes is as x, y, z , where the z -axis is the EM imaging direction.

Condition	Rat ID	Tissue size (voxel ³)	Voxel size (nm)	Tissue size (μm ³)
Sham	#25 contra	$2\,044 \times 4\,096 \times 1\,306$	$50 \times 50 \times 50$	$102.2 \times 204.8 \times 65.3$
	#25 ipsi	$4\,096 \times 2\,048 \times 1\,384$	$50 \times 50 \times 50$	$204.8 \times 102.4 \times 69.2$
	#49 contra	$4\,096 \times 2\,048 \times 1\,882$	$50 \times 50 \times 50$	$204.8 \times 102.4 \times 94.1$
	#49 ipsi	$2\,048 \times 2\,048 \times 1\,210$	$50 \times 50 \times 50$	$102.4 \times 102.4 \times 60.5$
TBI	#2 contra	$4\,096 \times 2\,048 \times 1\,086$	$50 \times 50 \times 50$	$204.8 \times 102.4 \times 54.3$
	#2 ipsi	$2\,154 \times 4\,134 \times 620$	$50 \times 50 \times 50$	$107.7 \times 206.7 \times 31.0$
	#24 contra	$4\,091 \times 2\,028 \times 1\,348$	$50 \times 50 \times 50$	$204.5 \times 101.4 \times 67.4$
	#24 ipsi	$2\,946 \times 2\,162 \times 1\,250$	$50 \times 50 \times 50$	$147.3 \times 108.1 \times 62.5$
	#28 contra	$4\,096 \times 2\,048 \times 1\,278$	$50 \times 50 \times 50$	$204.8 \times 102.4 \times 63.9$
	#28 ipsi	$4\,075 \times 2\,000 \times 1\,300$	$50 \times 50 \times 50$	$203.7 \times 100.0 \times 65.0$